Meta-analysis of experimental results for heat capacity and thermal conductivity in lithium-ion batteries: A critical review

Marco Steinhardt[a,*,#], Jorge V. Barreras[b,c,#], Haijun Ruan[c,d], Billy Wu[c,d], Gregory J. Offer[b,c], Andreas Jossen[a]

[a] *Technical University of Munich (TUM), Institute for Electrical Energy Storage Technology (EES),*
Arcisstrasse 21, 80333 Munich, Germany

[b] *Department of Mechanical Engineering, Imperial College London, London, UK.*

[c] *The Faraday Institution, Didcot, UK.*

[d] *Dyson School of Design Engineering, Imperial College London, London, UK.*

** Corresponding author: e-mail: marco.steinhardt@tum.de, telephone: +49 8928926967,*
fax: +49 8928926968

 # These authors contributed equally to this work.

Abstract

Scenarios with rapid energy conversion for lithium-ion batteries are increasingly relevant, due to the desire for more powerful electric tools or faster charging electric vehicles. However, higher power means higher cooling requirements, affecting the battery temperature and its thermal gradients. In turn, temperature is a key quantity influencing performance, safety and lifetime. Therefore, thermal models are increasingly important for the design and operation of battery systems. Key parameters are specific heat capacity and thermal conductivity. For these parameters, this paper presents a comprehensive review of the experimental results in the literature, where the median values and corresponding uncertainty are summarized. Whenever available, data is analyzed from component to cell level with the discussion of dependencies on temperature, state of charge (SOC) and state of health (SOH). This meta-analysis reveals gaps in knowledge and research needs. For instance, we uncover inconsistencies between the specific heat capacity of electrode-separator stacks and full-cells. For the thermal conductivity, we found that thermal contact resistance and dependencies on battery states have been poorly studied. There is also a lack of measurements at high temperatures, which are required for safety studies. Overall, this study serves as a valuable reference material for both modellers and experimenters.

Keywords: Li-ion battery, Heat capacity, Thermal conductivity, Thermal contact resistance

---

1. Introduction

In 1991, Sony released the first video camera powered by lithium-ion cells [1] - an energy storage technology that delivers nearly twice the energy density than nickel–metal hydride batteries (NiMH) [2]. Today, lithium-ion cells are still applied in consumer electronics, but their market share is increasingly shifting towards electric vehicles (EV) [3] and energy storage systems. This overall trend is set to continue supported by policies, regulations and technological advances [4].

One of the remaining technical challenges for lithium-ion batteries is the need to enhance their energy density and shorten charging time. However, as pointed out by Liu et al. [5], solving these challenges often results in thermal issues, i.e. a faster and non-uniform temperature increase. For example, Kraft et al. [6] observed that cells with a high-capacity cathode active material (lithium and manganese-rich) released up to four times as much heat during discharges compared to cells with a commonly used cathode active material (nickel-rich). On the other hand, Barreras et al. [7] showed that the problem of non-uniform temperatures during EV fast charging can be solved with innovative balancing concepts, but at the expense of additional cost and complexity, and the cooling needs are still significant.

Indeed, temperature is an important battery state that affects energy efficiency [8], ageing rates [9,10], electrical power capability [10] and the state of safety [11]. For instance, cell temperatures below -20 °C should be avoided for storage and operation as the electrolyte may begin to freeze [12,13]. Most lithium-ion cells can operate above -20 °C, but energy efficiency and the power capability are compromised. Especially high charging power induces accelerated aging due to lithium plating at low temperatures [9], which may even result in the formation and growth of lithium dendrites, leading to safety hazard, such as thermal runaway. It is widely accepted that the desired working temperature for lithium-ion cells starts between 10-20 °C and ends between 30-40 °C [12,14]. However, as demonstrated by Schimpe et al. [10], the optimal temperature range is not constant, but depends on the SOC, the C-rates, and the targeted aging rates. In addition, it was shown by Yang et al. [15] and Rodrigues et al. [16] that the cell design has also a strong influence on the optimal temperature range. In general, temperatures above the desired range and up to 60 °C should be avoided, because of their impairing effect on aging, such as the rapid growth of the solid-electrolyte interface (SEI) [9] and electrolyte depletion [17]. 60 °C constitutes a safety margin of 20 °C for the first exothermic reaction of the SEI, which starts between 80 and 120 °C [18–20]. This exothermic reaction can lead to the self-sustaining and safety-critical thermal runaway event.

Due to the significance of the cell temperature T_{cell} for safety, lifetime and performance, battery developers use thermal cell models. For these models, the specific heat capacity c_p at constant pressure constitutes an essential parameter. If thermal gradients inside the cell can be neglected (low Biot number), the lumped capacitance model in Equation (1) is a reasonable modeling approach for T_{cell} [21,22]. Accordingly, the increase in T_{cell} depends strongly on the specific heat capacity c_p, which is reviewed in this paper. Further influences on T_{cell} accrue from the density ρ, volume V_{cell}, and surface A_{surf} of the cell. On the operational side, the heat generation rate inside the cell $\dot{q}V_{cell}$, the heat transfer coefficient h_{surf}, and the ambient temperature T_{amb} act on T_{cell}. For adiabatic boundary conditions ($h_{surf} = 0$ W m^{-2} K^{-1}), uncertainties in c_p would translate directly into uncertainties in $\partial T_{cell}/\partial t$. For example, an uncertainty of 10% in c_p would cause an uncertainty in $\partial T_{cell}/\partial t$ of 10%, which can drop to an uncertainty of 6% at lower heat transfer coefficients (7 W m^{-2} K^{-1}) [23].

$$c_p \rho V_{cell} \frac{\partial T_{cell}}{\partial t} = \dot{q} V_{cell} - h_{surf} A_{surf} (T_{cell} - T_{amb}) \tag{1}$$

$$c_p \rho \frac{\partial T_{cell}}{\partial t} = k_x \frac{\partial^2 T_{cell}}{\partial x^2} + k_y \frac{\partial^2 T_{cell}}{\partial y^2} + k_z \frac{\partial^2 T_{cell}}{\partial z^2} + \dot{q} \tag{2}$$

If significant temperature gradients inside the lithium-ion cell are expected, thermal cell models usually apply a version of the heat Equation (2). For example, this can be the case for safety simulations [24], pre-heating studies [25], or fast charging investigation [26]. The thermal conductivity influences the temperature field T_{cell} in Equation (2), which depends on the location (x, y, z) and the time t. Due to the layered structure of the electrode-separator stack, the thermal conductivity is anisotropic and described by a value in each Cartesian direction (k_x, k_y, k_z). It should be noted that Equation (2) is expressed in Cartesian coordinates (x, y, z) but can readily be expressed in cylindrical coordinates (r, z, φ).

Equations (1) and (2) emphasize the dependency of T_{cell} on intrinsic material parameters of the cell (c_p, k_x, k_y, k_z) and the operational conditions $(\dot{q}, h_{surf}, T_{amb})$. Despite the importance of material parameters for T_{cell}, review papers [2,27] summarizing their values are out of date. In 2011, Bandhauer et al. [2] analyzed the results of two thermal conductivity studies [28,29] and expressed the need for a better understanding of thermal contact resistances within full-cells and the lack for measurement data for cells with lithium-iron-phosphate (LFP) cathodes. Madani et al. [30] and Tang et al. [31] concentrated their reviews on the experimental methods rather than on the results. Shah et al. [27] published one of the most comprehensive reviews on thermal parameters in 2016. They summarized eleven experiments on material and six on full-cell level. Despite this increase in experiments since 2011, Shah et al. [27] considers the available data for thermal transport properties to be insufficient, so that further experiments are necessary to resolve the spread of the reported results and to identify rate-limiting thermal transport processes. Kantharaj et al. [32] published the latest review paper on thermal parameters in 2019. Based on ten thermal studies at the material level and nine at the full-cell level, they expressed the need to understand the relationship between thermal conductivity and particle size, shape and distribution. In addition, the thermal contact resistance within full-cells has to be further characterized according to Kantharaj et al. [32].

This paper extends the literature review by Shah et al. [27] and Kantharaj et al. [32] by a statistical summary of the measurement results for the specific heat capacity c_p and thermal conductivity k of lithium-ion cells and their components. The review is called meta-analysis because of the statistical procedures, which allows a more objective appraisal to the field [33]. The meta-analysis is limited to present-day lithium-ion cells with a liquid or gel electrolyte. Therefore, all-solid state cells are not considered. Furthermore, the experimental characterization methods are not described in detail, but will be examined in a future publication. This review paper aims to facilitate the parameterization of thermal cell models and to reveal missing measurements for experimental researchers. Accordingly, this review aims to:

- Summarize values for specific heat capacity and thermal conductivity and present corresponding uncertainty ranges and medians for thermal models.
- Discuss the dependencies of the thermal parameters on temperature, SOC and SOH.
- Identify knowledge gaps and research needs in the field of thermal parameters.

This review paper deals with the specific heat capacity in Section 2 and the thermal conductivity and thermal contact resistances in Section 3. Corresponding subsections are listed in Table 1. For the specific heat capacity, components inside lithium-ion cells are first analyzed. For this meta-analysis, we differentiate between porous (e.g. coatings), solid non-porous (e.g. current collectors), and fluid (e.g. electrolyte) components. Afterwards, the specific heat capacity of these components are compared with results made on electrode-separator stacks and full-cells. Section 3 commences with the thermal conductivity of the electrode-separator stack and full-cells, which is described by a value in through-plane and in-plane direction. While the in-plane conductivity is predominately determined by the layer thicknesses of the current collectors [34], the through-plane conductivity is influenced by the thermal conductivity of the stack layers and thermal contact resistances between them. Both influencing quantities for the through-plane conductivity are reviewed in the last two subsections.

Table 1 provides further information about the measurement and evaluation level for the thermal experiments and names the thermal model, where parameterization benefits from the respective subsection either through direct (Y_d) application of the parameter or indirectly through a calculation (Y_{ac}). For model definitions and instructions on how to select the thermal parameters for each thermal model, see the supplementary material.

Each thermal experiment can be divided into a measurement phase and an evaluation phase, with the latter using the measurement results to calculate the desired parameters such as the thermal conductivity. In some subsections, the measurement and evaluation level can be different. Subsection 2.3 can contain, for example, the specific heat capacity of a full-cell measurement, but the evaluation phase of which compensates for components other than the stack. In this case, the result is considered to be the specific heat capacity of the stack and not the full cell.

Table 1: Subsections in this review paper with the measurement and evaluation levels of the thermal parameters and the applicability for models with different levels of homogenization. Applicability is assessed for layer-resolved models (LRM [28,35,36]), component-resolved models (CRM [6,37]) with multiple domains for components such as the cell housing or stack, and single-domain models (SDM [38]) with a single volume for the entire cell.

Subsection	Measurement level	Evaluation level	Applicability to models		
			LRM	CRM	SDM
2.1 Heat capacity of porous components and electrolytes	Cell component	Cell component	Y_d	Y_{AC}	Y_{AC}
2.2 Heat capacity of solid non-porous components	Cell component	Cell component	Y_d	Y_{AC}	Y_{AC}
2.3 Heat capacity of electrode-separator stacks	Full-cell, stack	Stack	N	Y_d	Y_{AC}
2.4 Heat capacity of full-cells	Full-cell	Full-cell	N	N	Y_d
3.1 Conductivity of electrode-separator stacks and full-cells	Full-cell, stack	Full-cell, stack	N	Y_d	Y_{AC}
3.2 Conductivity of solid non-porous components	Cell component	Cell component	Y_d	Y_{AC}	Y_{AC}
3.3 Conductivity of porous components	Cell component	Cell component	Y_d	Y_{AC}	Y_{AC}
3.4 Contact resistances	Full-cell, stack	Cell component	Y_d	Y_{AC}	Y_{AC}

Y_d: Can be directly applied in the thermal model. Y_{AC}: Additional calculations are required for use in the thermal model. N: Cannot be applied in the thermal model.

2. Specific heat capacity

This section addresses various heat capacity experiments from component to full-cell level, which is illustrated in Figure 1. Full-cell measurement are needed if the internal cell construction is unknown whereas heat capacities of cell components are a must for thermal cell design studies [39]. In addition, layer-resolved thermal models [36,40,41] require the specific heat capacity at the component level, while lumped-capacitance or single-domain models are more conveniently parameterized with averaged capacities from full-cell measurements [42]. Therefore, heat capacity measurements at both full cell and component level are useful in battery research.

Calorimetric methods are mostly used to measure the specific heat capacity, which in principle measure the heat flow to the test object and the subsequent temperature increase. The most frequently used type of calorimeter is the differential calorimeter with a measurement uncertainty between 1.5% and 10% [43]. Measurements that are more precise can be achieved with adiabatic calorimeters, which offer an uncertainty of 0.05 to 2% [43]. Besides the calorimetric equilibrium methods, transient measuring regimes such as the hot disc method can be used to measure the specific heat capacity [44]. The advantage of transient methods is that more than one thermal parameter can be measured [44]. In the field of lithium-ion cells, thermal impedance spectroscopy is a prominent transient method for measuring the specific heat capacity [45–48].

Lithium-ion cells contain porous components with a porosity ϵ. These include the cathode and anode coatings and the separator, as shown on the left-hand side of Figure 1. The specific heat capacity of such porous materials c_{por} can be calculated with Equation (3) [13]. c_{por} depends on the specific heat capacity of the fluid c_{fluid} and solid phase c_{solid}, which are weighted by their mass fraction. Therefore, the volume fraction ϵ has to be multiplied with the density of the fluid ρ_{fluid} and solid phase ρ_{solid}. The bulk density ρ_{bulk} of the porous material is calculated with Equation (4).

$$c_{por} = \frac{c_{fluid}\rho_{fluid}\epsilon + c_{solid}\rho_{solid}(1-\epsilon)}{\rho_{bulk}} \tag{3}$$

$$\rho_{bulk} = \rho_{fluid}\epsilon + \rho_{solid}(1-\epsilon) \tag{4}$$

It should be emphasized that the solid phase of anode, cathode, and the separator is also a composite. According to Equation (5) and (6), the weight fractions $m_{scm,i}/\sum_i m_{scm,i}$, densities $\rho_{scm,i}$, and specific heat capacities $c_{scm,i}$ of solid composite materials can influence c_{solid} and ρ_{solid}. Anode and cathode coatings in lithium-ion cells typically consist of solid active particles, polymer binders and additives [49,50]. The solid phase of separators usually consists of microporous polymer membranes, non-woven fabric mats or inorganic composites [51]. These three separator categories can contain solid materials such as polyethylene terephthalate (PET), polypropylene (PP), polyethylene (PE), polyamide (PA), polyvinylchloride (PVC), polyester (PU), Al_2O_3, and SiO_2 [51–53].

$$c_{solid} = \sum_i \left(\frac{m_{scm,i}}{\sum_i m_{scm,i}} c_{scm,i} \right) \tag{5}$$

$$\rho_{solid} = \frac{\sum_i m_{scm,i}}{\sum_i (m_{scm,i}/\rho_{scm,i})} \tag{6}$$

The stack level in Figure 1 encompasses porous coatings, porous separator sheets, and non-porous current collector foils. These stack layers build the electrode-separator stack, which is wound to form the so-called jelly roll in case of cylindrical cell formats. The effective heat capacity of the electrode-separator stack c_{stack} is defined by Equation (7) [54], which is independent of the geometry. Instead, the mass of the dry anode and cathode coatings (m_{ano}, m_{cat}), the mass of the anode and cathode current collectors (m_{anoCC}, m_{catCC}), and the mass of the dry separator m_{sep} compared to the total mass of the stack m_{stack} determines the weighting of the heat capacities. The specific heat capacity of the separator c_{sep}, anode coating c_{ano} and cathode coating c_{cat} are dry porous heat capacities c_{por} in the sense of Equation (3). Whereas the heat capacity of the anode c_{anoCC} and cathode c_{catCC} current collector in Equation (7) are solid non-porous heat capacities. It should be noted that all of the masses in Equation (7) must include passive components such as the excess of the separator or the overhang of the anode electrode. For example, the area of the anode can exceed the area of the cathode by 9%, which reduces the risk of lithium plating on the edges of the electrode [55].

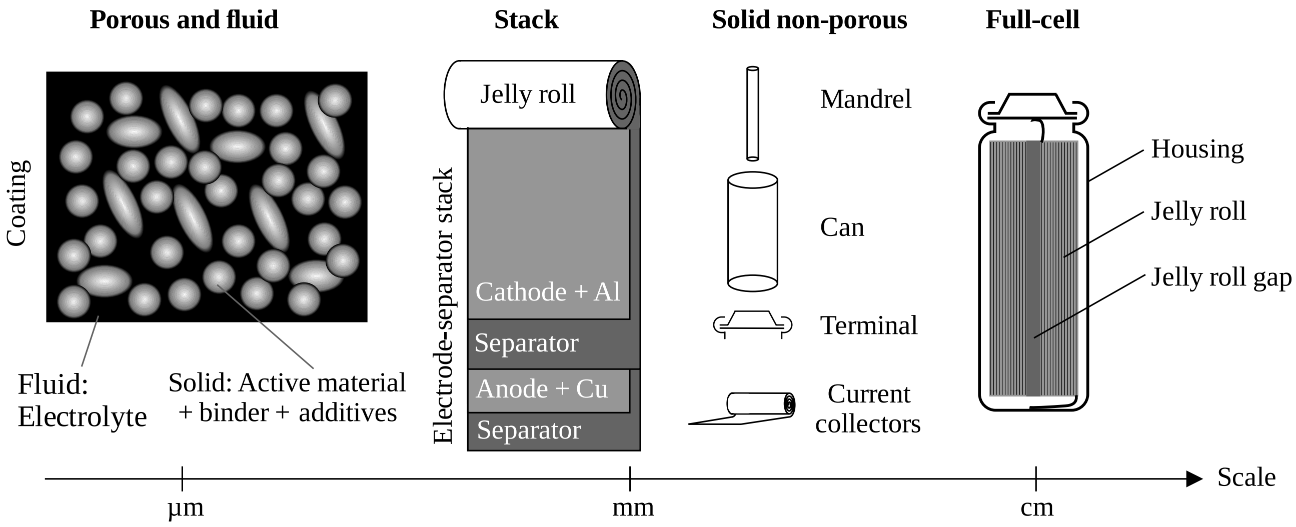

Figure 1: Schematic of different scales for the specific heat capacity demonstrated for the cylindrical cell format.

Besides the current collectors, full-cells contain further solid non-porous components in the cell housing such as the can and the terminal. Especially for cylindrical cells, the positive terminal can contain various subcomponents such as the current interrupt device (CID) [56]. Furthermore, some cylindrical cells contain a mandrel inside the jelly roll gap, which is used during the winding process. The specific heat capacity of the solid components outside the electrode stack c_n and their mass m_n introduce a difference between the heat capacity of the full-cell c_{cell} (Equation (8)) and c_{stack}.

$$c_{stack} = \frac{m_{ano}c_{ano} + m_{cat}c_{cat} + m_{sep}c_{sep} + m_{aCC}c_{aCC} + m_{cCC}c_{cCC} + m_{ele}c_{ele}}{m_{ano} + m_{cat} + m_{sep} + m_{aCC} + m_{cCC} + m_{ele}} \tag{7}$$

$$c_{cell} = \frac{m_{stack}c_{stack} + \sum_n (c_n m_n)}{m_{stack} + \sum_n (m_n)} \tag{8}$$

The specific heat capacities covered by Equations (3) to (8) are reviewed in the following subsections. Values for c_{solid} and c_{fluid} from Equation (3) are analyzed in subsection 2.1, which determines c_{ano}, c_{cat} and c_{sep}. Heat capacities for the current collectors (c_{aCC}, c_{cCC}) can be found in subsection 2.2. Subsections 2.3 and 2.4 cover direct measurements of c_{stack} and c_{cell}, respectively.

2.1. Heat capacity of porous components and electrolytes

Table 2 lists experimental results for porous c_{por} and fluid c_{fluid} materials used in lithium-ion cells and differentiates between whether the pores contain electrolyte (wet) or inert gas (dry). The mass fraction of the fluid phase $\rho_{fluid}\epsilon/\rho_{bulk}$ becomes negligible compared to the solid phase if inert gas such as argon fills the pores. Therefore, dry c_{por} can be equated with c_{solid} in Equation (3). Most dry test samples in Table 2 were extracted from commercial electrodes and washed and dried afterwards to remove any remainders of the electrolyte [13]. If the test sample was measured right after the dissection or additional electrolyte was added before the measurement, the experiment is labeled wet. Table 2 further contains information on ρ_{solid}, ρ_{bulk}, and ϵ, which characterizes the composition and morphology.

If a reference contains more than one measurement point for c_p, Table 2 lists the mid-range, which is the arithmetic mean of minimum and maximum. Changes in c_p can arise from many sources such as measurement uncertainty or variations in battery states such as SOC, SOH or temperature T. If the reference varies the temperature, this variation is also stated in Table 2 [54] by the mid-range and the deviation to the extrema. Furthermore, in case of varying temperature the temperature dependency $\alpha_{c_p,T}$ is fitted with a linear function: $p_1(T - 300\text{ K}) + p_2$. The temperature dependency is then defined by dividing the slope $p_1 = dc_p/dT$ with the heat capacity at 300 K ($p_2 = c_p(300\text{K})$). As the SOH has not been mentioned by any reference and the SOC is only mentioned by Gotcu et al. [57], Loges et al. [13], and Liebig et al. [58], both states are not included in the header of Table 2.

Table 2: Measured specific heat capacity of porous electrode coatings and separators c_{por}, and electrolytes c_{fluid} applied in electrode-separator stacks of lithium-ion cells. All electrode coatings contain active material, binder and conductive additives. If electrolyte is contained inside the pore, the measurement is declared wet. Dry measurements contain inert gas inside the pores, which equates c_{por} with c_{solid}. No information provided is marked with (-).

No.	Ref.	Stack layer	Dry / wet	$\frac{\rho_{solid}}{\text{g cm}^{-3}}$	$\frac{\rho_{bulk}}{\text{g cm}^{-3}}$	$\frac{\epsilon}{\%}$	$\frac{T}{\text{K}}$	$\frac{c_p}{\text{J kg}^{-1}\text{ K}^{-1}}$	$\frac{\alpha_{c_p,T}{}^{a)}}{\%\text{ K}^{-1}}$
1	[13]	Graphite $^{b)}$	Dry	2.31	-	46	283 ±50	710 ±151	+0.4

2	[13]	Graphite b)	Dry	2.31	-	47	283 ±50	715 ±149	+0.4
3	[13]	Graphite b)	Dry	2.44	-	53	283 ±50	696 ±154	+0.4
4	[13]	Graphite b)	Dry	2.15	-	51	283 ±50	718 ±139	+0.4
5	[13]	Graphite b)	Dry	2.01	-	66	283 ±50	720 ±147	+0.4
6	[13]	Graphite b)	Dry	2.46	-	43	283 ±50	729 ±149	+0.4
7	[59]	Graphite	Dry	-	1.621	-	323 ±30	1134	0.0
8	[54]	Graphite	Wet	-	1.35	-	-	1437	-
9	[58]	Graphite b)	Wet	-	-	31	326 ±28	1097 ±178	+0.8
10	[60]	Graphite b)	Wet	-	2.5	-	-	700	-
11	[13]	Separator b) d)	Dry	-	-	-	283 ±50	1786 ±436	+0.5
12	[13]	Separator b) d)	Dry	-	-	-	283 ±50	1614 ±345	+0.4
13	[13]	Separator b) d)	Dry	-	-	-	283 ±50	1581 ±337	+0.4
14	[13]	Separator b) d)	Dry	-	-	-	283 ±50	1234 ±239	+0.4
15	[13]	Separator b) d)	Dry	-	-	-	283 ±50	1583 ±367	+0.4
16	[13]	Separator b) d)	Dry	-	-	-	283 ±50	1600 ±381	+0.5
17	[13]	Separator e)	Dry	-	-	-	283 ±50	1583 ±340	+0.4
18	[13]	Separator e)	Dry	-	-	-	283 ±50	1683 ±340	+0.4
19	[13]	Separator f)	Dry	-	-	-	283 ±50	1556 ±354	+0.5
20	[59]	Separator	Dry	-	0.586	-	323 ±30	3250	0.0
21	[61]	Separator b)	Dry	-	0. 91	-	311 ±13	2475 ±5	0.0
22	[54]	Separator	Wet	-	1.01	-	-	1978	-
23	[58]	Separator b)	Wet	-	-	40	326 ±28	1689 ±141	+0.3
24	[60]	Separator b)	Wet	-	1.2	-	-	700	-
25	[13]	LCO b)	Dry	4.81	-	31	283 ±50	697 ±98	+0.3
26	[13]	LCO b)	Dry	4.48	-	29	283 ±50	707 ±98	+0.3
27	[57]	LCO c)	Dry	4.54	2.35	46 ±3	423 ±150	830 ±156	+0.1
28	[62]	LCO/LMO	Dry	4.72	2.34	48	436 ±138	862 ±119	+0.1
29	[54]	LCO	Wet	-	2.33	-	-	1269	-
30	[13]	NMC b)	Dry	3.88	-	37	283 ±50	767 ±95	+0.2
31	[13]	NMC b)	Dry	3.93	-	22	283 ±50	761 ±89	+0.2
32	[13]	NMC b)	Dry	4.24	-	36	283 ±50	764 ±94	+0.2
33	[57]	NMC c)	Dry	4.32	2.45	42 ±4	423 ±150	898 ±144	+0.1
34	[59]	NMC	Dry	-	2.580	-	323 ±30	1068	0.0
35	[58]	NMC b)	Wet	-	-	29	326 ±28	952 ±39	+0.2
36	[13]	LCO/NCA b)	Dry	3.93	-	23	283 ±50	737 ±99	+0.3
37	[63]	LFP c)	Dry	1.65	-	-	290 ±100	735 ±181	+0.2
38	[62]	LCO/LMO c)	Dry	3.96	1.73	58	436 ±138	904 ±92	+0.1
39	[60]	LMO b)	Wet	-	1.5	-	-	700	-
40	[13]	Electrolyte g)	-	-	1.28	-	293 ±40	1639 ±58	+0.1
41	[13]	Electrolyte h)	-	-	1.24	-	283 ±50	1630 ±74	+0.1
42	[54]	Electrolyte	-	-	1.130	-	-	2055	-
43	[59]	Electrolyte g)	-	-	1.280	-	323 ±30	229	0.0

a) The temperature dependency $\alpha_{c_p,T}$ is determined by dividing the slope of the linear regression $\partial c_p/\partial T$ by the heat capacity at 300 K.

b) Extracted from a commercially available lithium-ion cell. c) Weight fraction of the active material greater than or equal to 90%. d) Contains PP. e) Manufactured by Celgard. f) Manufactured by Toray. g) LP30 from BASF. h) LP50 from BASF

The bar chart in Figure 2 a) gives an overview of the 43 test samples in Table 2. Furthermore, the chart differentiates between wet and dry measurements. According to Figure 2 a), every common cathode chemistry of lithium-ion cells is contained in Table

2 except for lithium-nickel-cobalt-aluminum-oxide (NCA). Note that LCO/NCA is a blended cathode. Uncertainties in the heat capacity can be estimated for electrolyte, graphite (G), lithium-cobalt-oxide (LCO), lithium-nickel-manganese-cobalt-oxide (NMC) and separators because more than one test sample was measured. However, this uncertainty estimate is not possible for the frequently used cathode material LFP or LMO because only one test sample was measured. On the anode side, no experiments have been conducted for lithium-titanate-oxide (LTO) and silicon-graphite coatings [13]. Note that the coating includes the active material, binder and additives and not the current collector. The amount of data for graphite, LCO, NMC and the separator material allows comparisons between dry and wet measurements, with which the validity of Equation (3) can be checked. For this reason, the porosity ϵ of the material is listed in Table 2.

Figure 3 a) shows the boxplot of selected specific heat capacities with more than one entries in Table 2. In this review paper, the median is considered the recommended value for the thermal parameters, as it is the better choice in the case of skewed data or data with outliers [64]. First, the electrolyte is analyzed as the only non-porous material in Figure 3 a) with a median heat capacity of 1635 $\mathrm{J\ kg^{-1}\ K^{-1}}$. This median heat capacity can be explained by common electrolyte constitutes such as ethylene carbonate (EC, 1521 $\mathrm{J\ kg^{-1}\ K^{-1}}$ [65]) or dimethyl carbonate (DMC, 1855 $\mathrm{J\ kg^{-1}\ K^{-1}}$ [66]). As with solid composite materials, the specific heat capacity of liquid mixtures can be calculated using the weighted average in Equation (3) [67]. For example, the electrolyte LP30 (Table 2, No. 40) contains the carbonates EC and DMC [13] in equal weight fractions, which results in an average heat capacity of 1688 $\mathrm{J\ kg^{-1}\ K^{-1}}$ using Equation (3). This represents a slight deviation from the measured median of 3%.

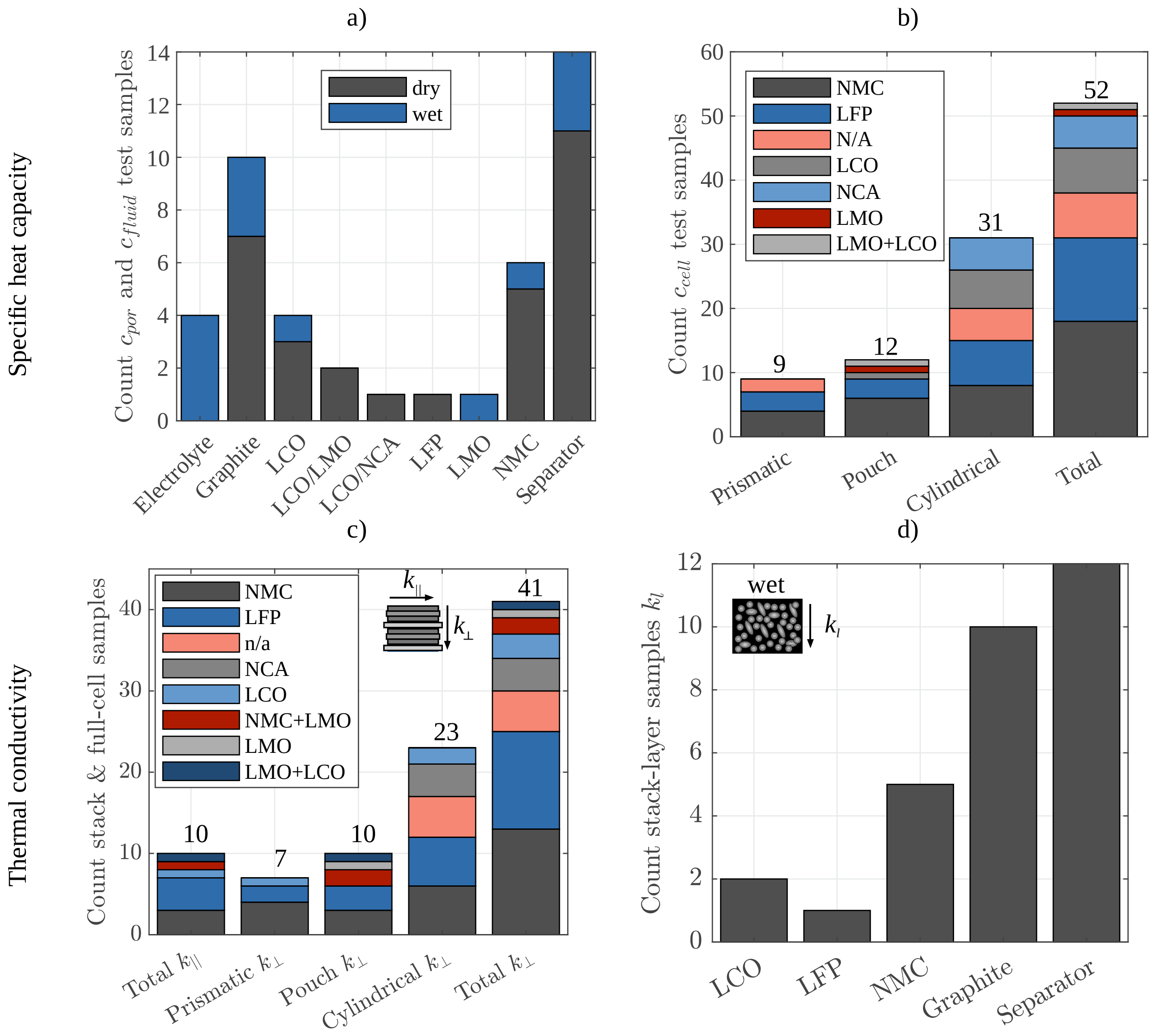

Figure 2: Number of test samples that were subjected to specific heat capacity and thermal conductivity experiments in the field of lithium-ion cells. a) Porous components c_{por} and the electrolyte c_{fluid} used for the electrode-separator stack, which are listed in Table 2. The legend differentiates between test samples with an electrolyte inside the pores (wet) and dry test samples. b) Full-cell test samples c_{cell} filtered by the cell format and cathode chemistry from Table 6. c) Number for full-cell or stack samples in the in-plane $k_{\parallel}$ (Table 8) or through-plane $k_{\perp}$ (Table 9) directions of the electrode-separator stack. Each bar shows the count of the cathode chemistry used for the test sample. d) Number of wet stack layer samples k_l, which are listed in Table 11.

The boxplot in Figure 3 a) shows a lower and upper whisker of 229 and $2055\ \mathrm{J\ kg^{-1}\ K^{-1}}$ for the electrolyte, which constitute a deviation of ±80% from the mid-range. Especially the lower whisker (LP30, Table 2, No. 43) has to be treated with caution, due to its low capacity compared to the electrolyte constitutes. Therefore, more electrolyte experiments are required to identify outliers and narrow the range for the heat capacity. In addition, the influence of the $LiPF_6$ salt on the heat capacity of the electrolyte c_{fluid} has not yet been investigated. As the mass fraction of $LiPF_6$ in common electrolytes lies around 10% (LP30 11.5 wt.% [68]), a significant impact on c_{fluid} cannot be neglected.

The boxplot in Figure 3 a) shows a median heat capacity of $1600\ \mathrm{J\ kg^{-1}\ K^{-1}}$ for dry separator sheets. This median agrees well with common raw materials of separators [52] such as PET ($1172\ \mathrm{J\ kg^{-1}\ K^{-1}}$ [69]), PE ($1549\ \mathrm{J\ kg^{-1}\ K^{-1}}$ [70]), and PP ($1634\ \mathrm{J\ kg^{-1}\ K^{-1}}$ [70]). According to the boxplot, No. 14 in Table 2 can be treated as an outlier, since the value of $1234\ \mathrm{J\ kg^{-1}\ K^{-1}}$ is below the lower whisker but a high weight fraction of PET could explain this result. On the upper side, No. 20 and 21 exceeds the upper whisker. In particular, the maximum of $3250\ \mathrm{J\ kg^{-1}\ K^{-1}}$ measured for a polyolefin separator does not correspond to the specific heat capacity of conventional polymers at 300 K [71]. In addition, inorganic separator materials such as Al_2O_3 or SiO_2 with a specific heat capacity of 866 and $746\ \mathrm{J\ kg^{-1}\ K^{-1}}$ [67] cannot serve as an explanation for the upper outlier. After the outliers have been identified, a value range for dry separators between 1556 and $1786\ \mathrm{J\ kg^{-1}\ K^{-1}}$ can be derived from the lower and upper whiskers of the boxplot. The corresponding mid-range of $1671\ \mathrm{J\ kg^{-1}\ K^{-1}}$describes the specific heat capacity of dry separators with an uncertainty of ±7%.

The cathode coatings NMC and LCO show similar heat capacities with a median of 767 and $707\ \mathrm{J\ kg^{-1}\ K^{-1}}$, respectively. Because of this slight deviation, there is no need to differentiate between the two cathode coatings according to Loges et al. [13]. This statement also seems to apply to LFP coatings with a specific heat capacity of $735\ \mathrm{J\ kg^{-1}\ K^{-1}}$ (Table 2, No. 37). For LFP and LMO, however, further measurements are required to clarify the question of whether differences in the heat capacity of lithium-ion cells can be explained by the cathode material. All of the dry cathode coatings in Table 2 have a median heat capacity near NMC of $764\ \mathrm{J\ kg^{-1}K^{-1}}$. Taking into account the lower and upper whiskers, the mid-range heat capacity for all cathodes contains an uncertainty of ±13%.

The median for dry graphite coatings is 718 $\mathrm{J\,kg^{-1}\,K^{-1}}$ in Figure 3 a), which contains the measurement results of seven test samples. Although these coatings contain polyvinylidene fluoride (PVDF) binder (1114 $\mathrm{J\,kg^{-1}\,K^{-1}}$ [72]) and carbon black (650 $\mathrm{J\,kg^{-1}\,K^{-1}}$ [72]), the median of 718 $\mathrm{J\,kg^{-1}\,K^{-1}}$ is close to pure graphite with a specific heat capacity of 706.9 $\mathrm{J\,kg^{-1}\,K^{-1}}$ [73]. The increase compared to pure graphite depends on the weight fraction of the binder. For example, a weight fraction of the PVDF binder of 5% [6] would increase the heat capacity of the graphite coating to 727 $\mathrm{J\,kg^{-1}\,K^{-1}}$. Given the composition of graphite coatings in lithium-ion cells, the heat capacity of 1134 $\mathrm{J\,kg^{-1}\,K^{-1}}$ (Table 2, No. 7) is most likely an outlier, which is supported by the boxplot calculations. The mid-range capacity of dry graphite exhibits a minor uncertainty of ±2% compared to other materials in Figure 3 a). The comparable lower uncertainty can be explained by the instance that all measurements contained in the median of 718 $\mathrm{J\,kg^{-1}\,K^{-1}}$ are conducted by Loges et al. [13]. Therefore, the ±2% range does not cover any other sources of uncertainty (e.g. measurement technique), which requires additional measurements in this field.

Using Equation (3) and (4) and the parameters in Table 2 to calculate c_{por} of wet coatings or separators can cause an uncertainty of up to 4%. This can be demonstrated by the experiments of Liebig et al. [58], because they indicated the porosity of the wet separator and the graphite coating (Table 2, No. 9, 23). For the demonstration, the median in Figure 3 a) of dry graphite (c_{solid}) and the median of the electrolyte (c_{fluid}), a solid and fluid density of 2.31 and 1.28 $\mathrm{g\,cm^{-3}}$ (Table 2, No. 1, 40), and a porosity of 31% are used. These values result in a heat capacity of the wet graphite coating of 901 $\mathrm{J\,kg^{-1}\,K^{-1}}$, which deviates by 2% from the measured capacity at 300 K (Table 2, No. 9). For the separator, a solid density of PP (0.89 $\mathrm{g\,cm^{-3}}$ [71]) is assumed, since the heat capacity of PP comes closest to the median of the separators in Figure 3 a). With a porosity of 40%, the heat capacity of the wet separator is calculated according to Equation (3) as 1617 $\mathrm{J\,kg^{-1}\,K^{-1}}$. This result for c_{por} corresponds to the measurement at 300 K with an uncertainty of 4% (Table 2, No. 23). Therefore, Equation (3) and (4) and Table 2 can be used as a powerful tool for determining the heat capacity of porous components of lithium-ion cells, if the researcher knows the porosity.

In general, the specific heat capacity at constant pressure c_p depends on the specific heat capacity at constant volume, the thermal expansion, the molar volume and the compressibility of the material - all variables with a temperature dependence [74]. The heat capacity at constant volume can be determined with quantum mechanical calculations. For example, taking into account the vibrations of atoms, Einstein formulated an equation for the capacity at constant volume, which depends on the temperature [75]. Often no measurement data for the entire temperature range are given for compressibility [74], which makes solid-state physical calculations of the temperature dependency of c_p more difficult. Therefore, measured temperature dependencies for c_p are discussed without physical calculations in this review paper.

Figure 3 b) shows the boxplot for the temperature dependency $\alpha_{c_p,T}$ listed in Table 2. As in Figure 3 a), the ordinate of the box plot in Figure 3 b) indicates the median of the temperature dependence in round brackets. According to the boxplot, the temperature dependency is positive for each material, with the lowest median being determined for the electrolyte (0.1% K^{-1}) and the highest for the wet graphite coating (0.8% K^{-1}). The boxplot in Figure 3 b) contains only a single wet test sample for the separator and graphite, since Liebig et al. [58] is the only study that measured wet heat capacities at different temperatures. Therefore, the identification of outliers and the assessment of uncertainties for both materials is not possible. Nevertheless, the plausibility can be verified by comparing wet and dry temperature dependencies. According to Equation (3) and assuming a linear dependency, $\alpha_{c_p,T}$ for wet materials has to lie between the electrolyte and the corresponding dry material. This is the case for the wet separator in Figure 3 b) but not for the wet graphite (Table 2, No. 9), which exceeds the temperature dependency of the dry coating by 0.4% K^{-1}. Therefore, further measurements are needed to clarify this discrepancy.

According to Figure 3 b), dry separator material has a temperature dependency of 0.4% K^{-1}, which corresponds well to PP material. The heat capacity of PP increases from 1570 to 1920 J kg^{-1} K^{-1} for a temperature increase from 273 to 323 K [67]. This change in heat capacity divided by the heat capacity at 300 K of 1622 $\mathrm{J\,kg^{-1}\,K^{-1}}$ [71] gives a consistent temperature dependence of 0.4% $\mathrm{K^{-1}}$. The consistency supports the suggestion of outliers in Figure 3 b) for temperature dependencies around 0.0% $\mathrm{K^{-1}}$. On the cathode side, LCO and NMC coatings show similar temperature dependencies of 0.2% $\mathrm{K^{-1}}$, which also correspond to LFP and LMO (Table 2 No. 37, 38). In contrast, graphite coatings show a higher temperature dependency of 0.4% $\mathrm{K^{-1}}$ with one outlier that found no dependence (Table 2, No. 7). As with separators, the temperature dependence of dry graphite coatings corresponds very well to that of pure graphite of 0.4% $\mathrm{K^{-1}}$ [73].

Most of the investigations in Table 2 neither mention the SOC after the electrodes have been extracted from a full-cell nor the electrode lithiation degree in the case of in-house electrode manufacture. Exceptions are the test series of Loges et al. [13], Liebig et al. [58], and Gotcu et al. [57]. Most of the results of Loges et al. [13] and Liebig et al. [58] were conducted at a full-cell SOC of 0%, while Gotcu et al. [57] used an electrode lithiation degree of 100%. In addition, Loges et al. [13] varied the full-cell SOC between 0% and 100% of a commercial graphite and LCO/NCA coating. According to their results, the specific heat capacity of the dry graphite coating increases with increasing full-cell SOC by 19%. In contrast, the LCO/NCA cathode coating decreased by 7% when the full-cell SOC was changed from 0% to 100%. As a result, the specific heat capacity of the electrode-separator stack can rise or fall, which is discussed in Subsection 2.3. Loges et al. [13] did not provide any physical explanations for the SOC dependence, but the Kopp-Neumann law [75] could explain their observation. This law says that the effective heat capacity of a compound depends on its atomic mass fraction and the heat capacity of the components. Since lithium (3582 $\mathrm{J\,kg^{-1}\,K^{-1}}$ [76]) has a higher specific heat capacity than all intercalation hosts used in lithium-ion cells, the heat capacity of the active material must increase with the degree of lithiation. Nevertheless, there should be no connection between the heat capacity and the SOC in full-cells, since the lithium content is retained for this control volume. Finally, it should be mentioned that the investigations in Table 2 do not reveal any details or variations in the SOH.

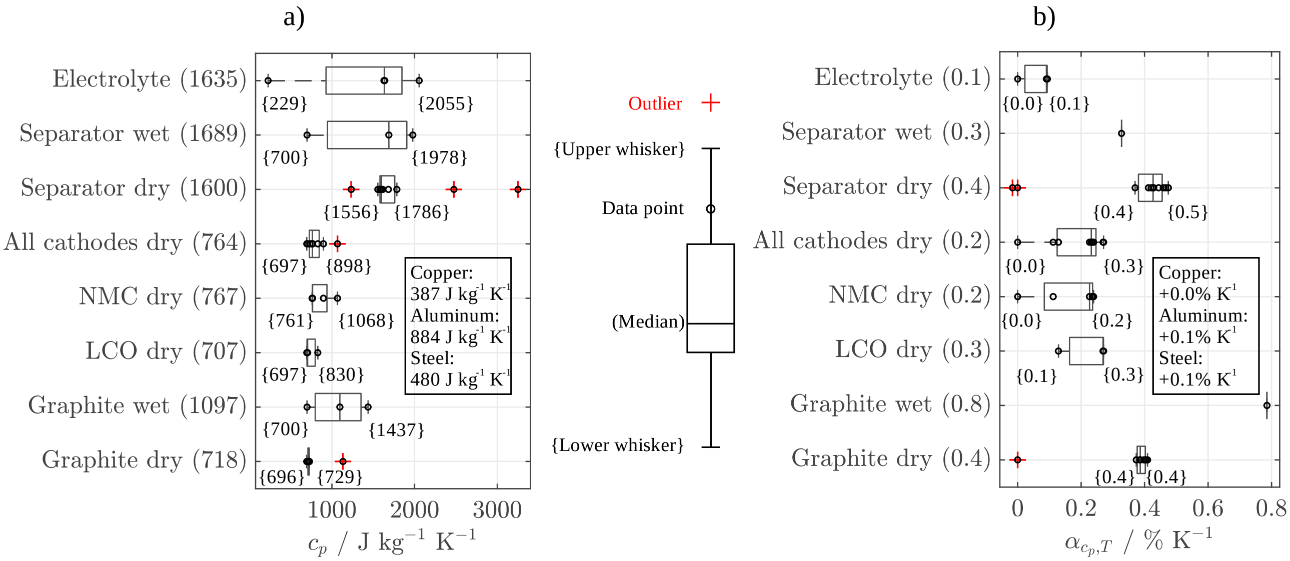

Figure 3: Specific heat capacity of components used in lithium-ion cells, with recommended values for thermal modeling in round brackets (median). a) Boxplot for c_{por} (wet), c_{solid} (dry) and c_{fluid} (electrolyte), which are listed in Table 2. Specific heat capacities of selected non-porous components from Table 3 are given in the square box. b) Boxplot of the linear temperature dependence of the specific heat capacity $\alpha_{c_p,T}$ from Table 2. SOC and SOH dependency is not include due to the small data quantity.

2.2. Heat capacity of solid non-porous components

A working lithium-ion cell not only contains porous and fluid components introduced in the previous subsection, but also solid non-porous components. To complete the electrode-separator stack in Figure 1, for example, the non-porous current collectors for the anode and cathode are necessary, which are usually made of copper and aluminum [13,77]. Furthermore, in order to determine the heat capacity of a complete lithium-ion cell, other non-porous components such as the cell housing must be taken into account. In the case of pouch cells, the cell housing consists of the pouch foil, a composite of aluminum, polyamide and polyethylene (PE) [13]. Prismatic cell housings are usually made of aluminum alloys [77,78] or stainless steel [50]. Pouch and prismatic cell formats also have external current collectors made of copper and aluminum [36,38]. This is not the case for cylindrical cells where the housing acts as the negative or positive current collector. Usually stainless steel is applied for the housing of cylindrical cells [79] and the terminal of the top cap. Besides the housing and the external terminals, lithium-ion cells can contain other components such as the CID [56], electrical insulation layers [78] or mandrels inside the jelly roll [80]. All consist of the materials listed in Table 3 with their specific heat capacity, which are important parameters in order to determine the total specific heat capacity of a lithium-ion cell.

Pure copper has the lowest specific heat capacity in Table 3 of $387\,\mathrm{J\,kg^{-1}\,K^{-1}}$. Furthermore, the temperature dependency $\alpha_{c_p,T}$ is negligible. In contrast, pure aluminum exhibit a small positive temperature dependency. Furthermore, the specific heat capacity of $884\,\mathrm{J\,kg^{-1}\,K^{-1}}$ is approximately twice the magnitude of copper. Both heat capacities are well predictable by the Dulong–Petit law [81], which states that the molar heat capacity of solid elements c_m is equal to three times the universal gas constant ($c_m = 3 \cdot 8.314\,\mathrm{J\,mol^{-1}\,K^{-1}}$). Three times the gas constant divided by the molar masses of copper ($63.5\,\mathrm{g\,mol^{-1}}$ [76]) and aluminum ($27.0\,\mathrm{g\,mol^{-1}}$ [76]) gives a specific heat capacity of 393 and $923\,\mathrm{J\,kg^{-1}\,K^{-1}}$, respectively. Both predictions of the Dulong–Petit law show a deviation of 2% and 4% from the mid-range heat capacity in Table 3.

Table 3: Measured specific heat capacity of solid components outside the electrode-separators stack c_n and the current collectors (c_{aCC}, c_{cCC}). No information provided is marked with (-).

Material	$\frac{\rho}{\mathrm{g\,cm^{-3}}}$	$\frac{T}{\mathrm{K}}$	$\frac{c_p}{\mathrm{J\,kg^{-1}\,K^{-1}}}$	$\frac{\alpha_{c_p,T}{}^{g)}}{\mathrm{\%\,K^{-1}}}$
Copper a)	8.96 [76]	316 ±18 [82]	387 ±2 [82]	+0.0
Aluminum b)	2.70 [76]	293 ±40 [83]	884 ±27 [83]	+0.1
Aluminum alloy 3003 c)	2.73 [84]	-	893 [84]	-
Pouch foil d)	-	283 ±50 [13]	1191 ±208 [13]	+0.3
PP e)	0.95 [70]	300 ±30 [70]	1634 ±188 [70]	+0.4
PET e)	1.35 ±0.05 [71]	300 ±30 [69]	1172 ±112[69]	+0.3
PE e)	1.00 [70]	300 ±30 [70]	1549 ±130 [70]	+0.3
Stainless steel AISI 304 f)	7.90 [85]	300 ±30 [86]	480 ±12 [86]	+0.1

a) Anode current collector, Negative cell terminal. b) Cathode current collector, Anode current collector (LTO) [87], Positive cell terminal. c) Prismatic cell housing [34,77,78], Cylindrical housing [45]. d) Aluminum polymer composite [13]. e) Pouch foil layer. f) Cylindrical housing [79,88], Prismatic cell housing [50], Cylindrical mandrel / center pin [80]. g) The temperature dependency $\alpha_{c_p,T}$ is determined by dividing the slope of the linear regression $\partial c_p/\partial T$ by the heat capacity at 300 K.

According to Table 3, pure aluminum and aluminum alloys have a similar heat capacity. For example, a frequently used aluminum alloy for prismatic housings is EN AW-3003 [34,78] that contains 1.5% Mn, 0.6% Si, and 0.7% Fe [89]. The heat capacity of pure aluminum and the alloy 3003 differs in Table 3 by only 1%. Because of this small difference, the established assumption [40] of pure aluminum for prismatic cell housings appears appropriate for thermal cell models. For pure aluminum, $\alpha_{c_p,T}$ shows a positive correlation between the temperature and c_p. No experiments that vary the temperature were found for the alloy 3003.

With regard to the heat capacity, polymers and aluminum equally influence pouch foils of lithium-ion cells. The pouch foil exhibits a specific heat capacity of $1191\ \mathrm{J\ kg^{-1}\ K^{-1}}$. This corresponds to a deviation of 35% compared to pure aluminum and 27% compared to the polymer PP in Table 3. However, pouch foils can also contain polymers other than PP. For example, the pouch foil AvALL158 (Avocet Steel Strip Ltd) suitable for electric vehicles with a total thickness of 158 µm contains PET (12 µm), adhesive (9 µm), polyamide PA (25 µm), aluminum (40 µm), and PP (70 µm). Similar ratios between the thickness of the polymer layer and the total thickness for the pouch foil were stated by Rheinfeld et al. [21] (72%) and Zhang et al. [90] (62%). Consequently, depending on the layer thickness and the polymers used in Table 3, the heat capacity of pouch foils can be between 884 and $1643\ \mathrm{J\ kg^{-1}\ K^{-1}}$. Because of this large range of $759\ \mathrm{J\ kg^{-1}\ K^{-1}}$, thermal models must take into account the exact construction of the pouch foil.

2.3. Heat capacity of electrode-separator stacks

Subsection 2.1 and 2.2 covered porous coatings, separator sheets and current collectors used in lithium-ion cells. These components form the electrode-separator stack, as shown in Figure 1. This subsection gives an overview of experiments measuring the specific heat capacity of the entire stack c_{stack} and compares the results with the two previous subsections. According to Equation (7), c_{stack} depends heavily on the mass fractions of the stack components, which are listed in Table 4 for some lithium-ion cells based on the total cell mass m_{cell}.

Regardless of the cell format in Table 4, the cathode coating has the largest mass fraction of the electrode-separator stack and therefore the greatest influence on c_{stack}. This is due to the high density of the cathode coatings, which is about twice that of graphite (see Table 2). The separator has the smallest mass fraction and therefore less influence on c_{stack}. Table 4 also contains the mass fraction of cell components outside the electrode-separator stack $(\sum m_n)/m_{cell}$, whose impact on c_{cell} will be discussed in the next subsection.

Due to the high mass fraction of the stack m_{stack}/m_{cell}, the heat capacity of the stack c_{stack} has a significant influence on the heat capacity of the full-cell c_{cell}. In the case of pouch cells, for example, the mass fraction is between 94% and 96% in Table 4, while cylindrical cells have a fraction between 73% and 86%. Despite the importance of c_{stack}, less measurement data is available in the literature. c_{stack} can be measured either at the stack level [13] or at the full-cell level, while the full-cell level requires compensation for the non-stack components [45,47]. Table 5 lists the results of both approaches with the nominal capacity of the full-cell Q_{cell}, the active materials of the stack, the SOC and the temperature T during the experiment, the specific heat capacity c_{stack} and the temperature dependency $\alpha_{c_p,T}$.

Table 4: Mass fractions of components within the electrode-separator stack and cell components outside the stack used in Equation (3) and (4) to calculate c_{stack} and c_{cell}. No information provided is marked with (-).

Ref.	$\frac{Q_{cell}}{\text{Ah}}$	$\frac{m_{cell}}{\text{g}}$	Format	Active material	$\frac{m_{cat}}{m_{cell}}$	$\frac{m_{ano}}{m_{cell}}$	$\frac{m_{ele}}{m_{cell}}$	$\frac{m_{aCC}}{m_{cell}}$	$\frac{m_{cCC}}{m_{cell}}$	$\frac{m_{sep}}{m_{cell}}$	$\frac{\sum m_n}{m_{cell}}$
[91]	2.6	44.3	Cylindr.	LCO/NMC-G	41%	18%	10%	7%	4%	3%	17%
[91]	1.5	43.1	Cylindr.	NMC-G	26%	15%	10%	17%	7%	3%	22%
[91]	1.1	39.0	Cylindr.	LFP-G	25%	13%	16%	10%	6%	3%	27%
[92]	3.35	45.4	Cylindr.	NCA-G	39%	26%	10%	6%	3%	2%	13%
[88]	7.5	320.0	Cylindr. a)	NCA-G	-	-	15%	-	-	5%	48%
[93]	41	865.0	Pouch b)	NMC/LMO-G	38%	25%	14%	10%	6%	4%	4%
[94]	-	791.0	Pouch	LCO/NCA-G	43%	21%	14%	9%	7%	2%	3%
[95]	3.8	88.2	Pouch	NMC-G	31%	17%	7%	24%	10%	7%	4%
[78]	8	328	Prismatic	LFP-G	-	-	15%	-	-	11%	16%

a) High-power type. b) High-energy type.

With the exception of NCA, all common cathode materials are represented in Table 5. Most references state the SOC, but only Cheng et al. [96] performed heat capacity measurements at different SOCs. In contrast to the temperature T, with a median of the mid-ranges of 303 K, no reference states the SOH. The results of Barsoukov et al. [47] in Table 5 seem to overestimate c_{stack} as all other investigations measure significant lower heat capacities. In addition, some results (Table 5, No. 2, 3, 5) even exceed the heat capacity of common electrolytes c_{ele}, which is not possible according to the weighted average in Equation (7) and heat capacity of the electrolyte c_{ele} in Figure 3.

Without the investigations of Barsoukov et al. [47], the median of all mid-ranges of c_{stack} in Table 5 amounts to 959 J kg^{-1} K^{-1}. This median lies within the heat capacity of the stack components from Figure 3 a). The comparison of No. 6 with 7 to 10 in Table 5 confirms that LCO coatings have a lower heat capacity than NMC, which was shown in Figure 3 a). In addition, c_{stack} only varies by ±77 J kg^{-1} K^{-1} (±8%), which could be caused by different stack designs (e.g. high energy or high power) or different battery states such as temperature.

According to Loges et al. [13], the porosity ϵ in general and the thickness ratio of the coating to the current collector of the anode d_{ano}/d_{aCC} have a dominant influence on c_{stack}. Due to its low mass fraction of 3% (median Table 4), the separator usually has a minor influence. In addition, dry cathode coatings and aluminum collectors have a similar heat capacity of 798 ±101 J kg^{-1} K^{-1}, which reduces the influence of variation in the cathode mass fractions on c_{stack}. On the other hand, No. 7 to 9 in Table 5 show that c_{stack} increases significantly with d_{ano}/d_{aCC}, which can be quantified by a linear correlation coefficient of +0.87. In contrast, the correlation with ϵ_{ano} is weaker with a linear correlation coefficient of +0.56. Because of the good correlation between d_{ano}/d_{aCC} and energy density [97], it is also expected that c_{stack} will correlate with energy density of the cell.

In addition to cell design parameters such as d_{ano}/d_{aCC}, battery states such as temperature can also cause differences in c_{stack}. The temperature dependency $\alpha_{c_p,T}$ of 0.2% K^{-1} of the stack corresponds with that of dry cathode materials in Figure 3 b), which can be explained by the high mass fraction of cathode coatings in Table 4. The SOC dependency $\alpha_{c_p,SOC}$ shows a declining heat capacity of -1% when the SOC is increased from 0% to 100%, which constitutes a weak correlation (Table 5, No. 10). Due to the lack of measurement data with varying SOH, the dependency of this battery state for c_{stack} is unknown.

Table 5: Measured specific heat capacity of electrode-separators stacks c_{stack} in lithium-ion cells. Every stack consists of two anode coatings, two cathode coatings, two separator sheets and one current collector for each electrode. Every porous layers of the stack is soaked in electrolyte (wet). No information provided is marked with (-).

No.	Ref.	Q_{cell} / Ah	m_{cell} / g	Active material	ϵ_{ano} / %	d_{ano} / d_{aCC}	SOC / %	T / K	c_{stack} / J kg^{-1} K^{-1}	$\alpha_{c_p,T}$ a) / % K^{-1}
1	[45]	4.4	194	LFP-G c)	-	-	50	303	958	-
2	[47]	1.8	42.7	-	-	-	100	296	1800	-
3	[47]	1.5	39.5	-	-	-	100	296	1900	-
4	[47]	1.3	41.6	-	-	-	100	296	1200	-
5	[47]	1.4	40.9	-	-	-	100	296	2400	-
6	[13]	6.8	-	LCO-G d)	46	17	0	303 ±30	882 ±65	+0.2
7	[13]	28	-	NMC-G c)	51	7	0	303 ±30	977 ±63	+0.2
8	[13]	50	-	NMC-G d)	43	10	0	303 ±30	985 ±68	+0.2
9	[13]	60	-	NMC-G d)	53	12	0	297 ±36	1036 ±74	+0.2
10	[96]	37	805	NMC-G	-	-	55 ±45 b)	308 ±20	953 ±42	+0.2
11	[98]	3.4	49.0	NMC-SiG d)	21	16	40 ±30 c)	300 ±15	1004 ±34	+0.2
12	[98]	4.8	69.0	NMC-SiG d)	30	16	43 ±28 c)	300 ±15	911 ±28	+0.2
13	[13]	3.2	-	LCO/NCA-G c)	66	4	0	303 ±30	976 ±52	+0.2

a) The temperature dependency $\alpha_{c_p,T}$ is determined by dividing the slope of the linear regression $\partial c_{stack}/\partial T$ by the heat capacity at 300 K. b) The SOC dependency $\alpha_{c_p,SOC}$ is determined by dividing the slope of the linear regression $\partial c_{stack}/\partial \text{SOC}$ by the heat capacity at a SOC of 50% amounts to -1%. c) High-power type. d) High-energy type. c) $\alpha_{c_p,SOC} = 0\%$

2.4. Heat capacity of full-cells

This subsection deals with the specific heat capacity of lithium-ion full-cells c_{cell} defined in Equation (8). As shown in Figure 1, c_{cell} is determined by the heat capacity of solid components outside the electrode-separator stack and c_{stack}, which were discussed in Subsection 2.2 and 2.3, respectively. According to the mass fractions $(\sum m_c)/m_{cell}$ in Table 4, components outside the stack can influence c_{cell} by up to 48%. Therefore, a strong impact on c_{cell} is very likely especially in the case of housings made of steel with a lower heat capacity of 480 J kg^{-1} K^{-1} (Table 3) compared to the stack c_{stack}. Pouch cells, on the other hand, have a mass fraction of approximately 4%, which indicates a smaller deviation between c_{stack} and c_{cell}.

Figure 2 b) shows the amount of heat capacity measurements that were carried out on full-cells. There are 52 experiments for c_{cell} in the literature, which are listed in Table 6. The cylindrical cell format is the most-studied format with 31 experiments followed by the pouch (12) and prismatic (9) format. In addition, Figure 2 b) differentiates the cathode chemistry of the full-cells. Accordingly, the cathodes NMC, LFP, NCA and LCO have been well researched, while only one experiment exists for LMO (Table 6, No. 42). A graphite coating was used on the anode side in most of the studies, but some used LTO (Table 6, No.42, 52). As at component level, anodes with silicon-graphite have not been measured so far in the literature.

The temperature T in Table 6 indicates the temperature during the measurement of c_{cell}. Using the median of all mid-ranges in Table 6 results in a temperature of 299 K and a SOC of 50%. In contrast to T and SOC, the SOH is rarely given in the references. Only Geder et al. [99] (No. 8), Bazinski et al. [100] (No. 38), and Vertiz et al. [101] (No. 40) provide information on the SOH during the measurement. Furthermore, the investigation of Geder et al. [99] is the only experiment with varying SOH. They did not observe any significant influence of SOH on c_{cell}.

It is important to examine the uncertainty of c_{cell} when calculating this parameter from the heat capacity of the cell components in Table 2 and Table 3. If a sufficiently low uncertainty can be achieved for the calculated c_{cell}, measurements on full-cells could be omitted if the researcher has sufficient information about the composition of the full-cell. One way to determine the uncertainty is to compare the measured and calculated value for c_{cell}. In Table 6, two references made this comparison. Sheng et al. [78] calculated a maximum deviation of 5% at 300 K from the measured c_{cell} (Table 6, No. 49), which is half the deviation of 9% observed by Vertiz et al. [101] (Table 6, No. 40). Hence, it seems possible to calculate c_{cell} with an uncertainty of 9%, but more research is needed to verify this uncertainty. Compared to the uncertainties of differential scanning calorimeters, which is between 1.5% and 5% depending on the calibration [43], there is no clear answer as to whether the calculation or the measurement is more accurate.

Table 6: Measured specific heat capacity of full lithium-ion cells c_{cell} according to Equation (8). No information provided is marked with (-).

No.	Ref.	$\frac{Q_{cell}}{\mathrm{Ah}}$	$\frac{m_{cell}}{\mathrm{g}}$	Format	Active material	$\frac{\mathrm{SOC}}{\%}$	$\frac{T}{\mathrm{K}}$	$\frac{c_{cell}}{\mathrm{J\ kg^{-1}\ K^{-1}}}$	$\frac{\alpha_{c_p,T}^{\mathrm{a)}}}{\%\ \mathrm{K^{-1}}}$	$\frac{\alpha_{c_p,SOC}^{\mathrm{b)}}}{\%}$
1	[48]	2	42.9	Cylindr.	-	-	293	1013	-	-
2	[48]	2.7	45	Cylindr. d)	-	-	293	907	-	-
3	[48]	1.1	39.4	Cylindr. c)	-	-	293	1011	-	-
4	[102]	-	-	Cylindr.	-	-	-	800	-	-

5	[103]	6	375	Cylindr. c)	-	-	-	795	-	-
6	[104]	5	96	Cylindr.	NMC	50	303	980 ±2	-	-
7	[105]	3.49	49	Cylindr.	NMC-G	-	298	1046	-	-
8	[99]	2.15	44	Cylindr. c)	NMC-G	50	316	851 ±9	-	-
9	[79]	2.4	44.7	Cylindr.	NMC	-	293 ±40	1047 ±115	+0.3	-
10	[79]	4.6	65.9	Cylindr.	NMC	-	293 ±40	1013 ±92	+0.2	-
11	[106]	2.25	42.3	Cylindr.	NMC-G	-	-	1100	-	-
12	[107]	4.15	67	Cylindr. d)	NMC-G	50	318 ±20	874 ±65	+0.4	-
13	[108]	4.4	82	Cylindr. d)	NMC-G	50 ±50	-	1314 ±31	-	5
14	[104]	2.5	76	Cylindr.	LFP	50	303	1148 ±21	-	-
15	[109]	-	-	Cylindr.	LFP	100	-	1720	-	-
16	[109]	-	-	Cylindr.	LFP	100	-	1605	-	-
17	[110]	2.5	70	Cylindr.	LFP-G	50 ±50	314 ±19	1117 ±36	+0.1	3
18	[106]	1.5	38.6	Cylindr.	LFP-G	-	-	1100	-	-
19	[111]	8	335	Cylindr.	LFP-G	-	-	998	-	-
20	[108]	2.5	70	Cylindr. c)	LFP-G	50 ±50	-	1139 ±14	-	2
21	[105]	3.57	48	Cylindr.	NCA-G	-	298	959	-	-
22	[105]	2.14	45	Cylindr.	LCO-G	-	298	1002	-	-
23	[29]	1.35	-	Cylindr.	LCO-G	-	315	1000 ±40	-	-
24	[112]	2.6	-	Cylindr.	LCO	-	288 ±10	893 ±79	-	-
25	[113]	1.35	40	Cylindr.	LCO-G	-	318 ±10	945 ±125	-0.7	-
26	[106]	2.6	44	Cylindr.	LCO-G	-	-	1100	-	-
27	[83]	0.5	19	Cylindr.	LCO-G	48 ±48	325 ±15	820 ±32	+0.1	-4
28	[110]	2.7	48	Cylindr.	NCA-G	50 ±50	313 ±18	830 ±19	+0.1	2
29	[114]	2.75	45	Cylindr.	NCA-G	-	283 ±30	1133 ±24	-0.0	-
30	[108]	2.7	48	Cylindr. d)	NCA-G	50 ±50	-	837 ±11	-	3
31	[108]	3.1	48.5	Cylindr. d)	NCA-SiG	50 ±50	-	1058 ±31	-	6
32	[104]	10	198	Pouch	NMC	50	303	1160 ±22	-	-
33	[115]	40	-	Pouch d)	NMC	-	298	860	-	-
34	[78]	9	222	Pouch	NMC	50	293 ±40	1093 ±113	+0.3	-
35	[116]	12	326.6	Pouch c)	NMC-G	-	-	1070	-	-
36	[117]	40	910	Pouch	NMC-G	-	315 ±17	1138 ±69	+0.3	-
37	[118]	37	560	Pouch	NMC-G	-	299	948	-	-
38	[100]	14	385	Pouch	LFP-G	50 ±50	298 ±30	1380 ±251	+0.5	4
39	[78]	9	235	Pouch	LFP	50	293 ±40	1085 ±105	+0.3	-
40	[101]	14	-	Pouch	LFP-G	50 ±50	-	1119 ±5	-	-1
41	[119]	2.28	-	Pouch	LCO-G	50 ±50	304	1091 ±45	-	7
42	[87]	-	-	Pouch c)	LMO-LTO	50 ±40	298	1056 ±12	-	0
43	[90]	25	1154	Pouch	LMO/LCO-G	-	300	1243	-	-
44	[104]	5	276	Prismatic	NMC	50	303	1025 ±13	-	-
45	[38]	43	840	Prismatic	NMC d)	50	298 ±15	933 ±39	+0.2	-
46	[120]	104	2032	Prismatic	NMC-G	50 ±50	333 ±8	1033 ±73	+0.3	7
47	[121]	43	840	Prismatic	NMC d)	50	296 ±23	978 ±3	+0.0	-
48	[46]	42	-	Prismatic	LFP-G	50	295	1142	-	-
49	[78]	8	328	Prismatic	LFP-G	50 ±50	293 ±40	1174 ±137	+0.2	4
50	[118]	20	610	Prismatic	LFP-G	-	299	1048	-	-
51	[22]	2.8	45	Prismatic	-	-	300	907 ±13	-	-
52	[121]	23	550	Prismatic	LTO c)	50	296 ±22	1146 ±11	+0.0	-

---

a) The temperature dependency $\alpha_{c_p,T}$ is determined by dividing the slope of the linear regression $\partial c_{cell}/\partial T$ by the heat capacity at 300 K. b) The SOC dependency $\alpha_{c_p,SOC}$ is determined by dividing the slope of the linear regression $\partial c_{cell}/\partial \mathrm{SOC}$ by the heat capacity at 50% SOC. c) High-power type. d) High-energy type.

Figure 4 a) shows a scatter plot of all data points listed in Table 6 if the temperature T is stated by the reference. Furthermore, the marker shape and color distinguish the cell format. If the SOC is stated by the reference, the marker face color is changed according to the gray-scale color bar. It can be seen that c_{cell} was measured between 250 K and 340 K, which can be viewed as the operating window for lithium-ion cells. No experiments for c_{cell} are available for safety simulations with temperatures above 340 K. In addition, there are no experiments below 250 K, which is still an operating temperature for military or aerospace applications [16].

The three horizontal lines in Figure 4 a) indicate a format dependency of c_{cell}. Comparing the medians of the mid-ranges shows a lower c_{cell} for cylindrical cells (912 $\mathrm{J\ kg^{-1}\ K^{-1}}$) than for prismatic (1041 $\mathrm{J\ kg^{-1}\ K^{-1}}$) and pouch cells (1168 $\mathrm{J\ kg^{-1}\ K^{-1}}$). The housing can explain the difference between the formats assuming the same values for c_{stack}. For example, cylindrical steel-housings have a lower heat capacity than prismatic aluminum-housings and aluminum has a lower heat capacity than pouch foils (see Table 3). The median value for c_{stack} of 959 $\mathrm{J\ kg^{-1}\ K^{-1}}$ in Table 5 is exceeded by the prismatic and the pouch format. This is a contradiction because the pouch foil does not have much influence and the heat capacity of prismatic housings is below 976 $\mathrm{J\ kg^{-1}\ K^{-1}}$.

There are several reasons that could explain a higher value in c_{cell} than c_{stack}. First, the stack design of the cells listed in Table 6 could be systematically different from the stacks listed in Table 5. For example, this would be the case if Table 5 only contains stacks of high-power cells and Table 6 contains only cells with a high-energy design. However, this is unlikely because Table 5 and Table 6 contain high-energy and high-power stacks and cells with a variety of cathode chemistries. Second, a higher electrolyte volume than the pore volume [122,123] could increase c_{cell} compared to c_{stack} due to the high heat capacity of the electrolyte. For example, An et al. [123] recommended an electrolyte volume of 190% of the pore volume to enable long-term cycling capability and low impedance. Third, measurement errors can be used as an explanation.

Nevertheless, the median of the pouch format deviates by 20% from $976\,\mathrm{J\,kg^{-1}\,K^{-1}}$, which exceeds the measurement uncertainty of common measurement methods [43]. In conclusion, more research is needed to clarify the discrepancy between c_{stack} and c_{cell} for pouch and prismatic cells.

The median of all temperature dependencies $\alpha_{c_p,T}$ of c_{cell} in Table 6 amounts to $+0.2\%\ \mathrm{K^{-1}}$. This value matches the temperature dependency of wet electrode-separator stacks in Table 5. The negative dependency of $-0.7\%\ \mathrm{K^{-1}}$ (Table 6, No. 25) can be treated as an outlier, since $\alpha_{c_p,T}$ of cell components lie within 0.0 and $0.4\%\ \mathrm{K^{-1}}$ according to Figure 3 b) and Table 3. For the SOC dependency $\alpha_{c_p,SOC}$, Table 6 lists values between -4% and 7% for c_{cell}, which is in the same order of magnitude as the 2% that Loges et al. [13] measured for c_{stack}.

Temperature and SOC can influence c_{cell}, but also design parameters such as the layer thicknesses have an influence. High energy cells usually have a higher ratio between the thickness of the active material and the current collectors (d_{ano}/d_{aCC}, d_{cat}/d_{cCC}). Loges et al. [13] pointed out that a thicker anode coating d_{ano} increases the specific heat capacity of the entire electrode because the low heat capacity of copper has less of an impact. Thus, an increase in d_{ano}/d_{aCC}, increases the specific heat capacity of the anode electrode. On the other hand, increasing d_{cat}/d_{cCC} has less of an impact on the cathode electrode, since most wet cathode coatings have a similar specific heat capacity as the aluminum current collector. This postulates a positive correlation between d_{ano}/d_{aCC} and c_{cell}, which implies a correlation between the energy density of the cell and c_{cell}.

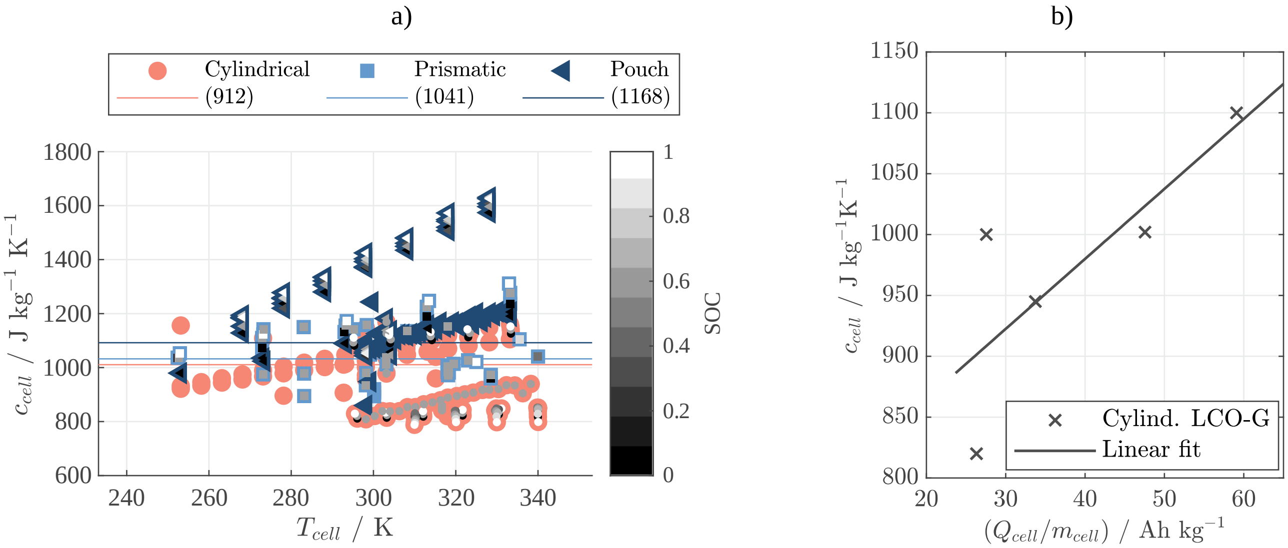

Figure 4: Dependencies of the full-cell heat capacity c_{cell} on operational and design parameters of lithium-ion cells. a) Format, temperature, and SOC dependency with the format medians in round brackets. Each marker represents one measurement result from the references in Table 6. The marker face color is chosen according to the grayscale color bar, if the reference states the SOC. b) Correlation between c_{cell} of cylindrical lithium-ion LCO-G cells with their specific electrochemical capacity Q_{cell}/m_{cell}.

With increasing coating thicknesses, the specific energy e_{cell} of the lithium-ion cell also increases. e_{cell} is often defined as the product of nominal voltage and electrical capacity divided by the cell mass $U_{cell}Q_{cell}/m_{cell}$. To examine the correlation between e_{cell} and c_{cell}, Figure 4 b) shows c_{cell} as a function of the specific capacity Q_{cell}/m_{cell} listed in Table 6. Since only the heat capacities of cells with an LCO cathode and a graphite anode are used, the x-axis of Figure 4 b) can be converted to e_{cell} by multiplying it with the nominal voltage of LCO-G (3.7 V [106]). In addition, only cylindrical cells are considered in order to reduce the influence of the cell housing on the correlation between e_{cell} and c_{cell}. The remaining data points are approximated in Figure 4 b) using a linear regression. As postulated, the slope of the linear regression has a positive value of 5.8 J K^{-1} Ah^{-1} with a 95% confidence interval of ±8.1 J K^{-1} Ah^{-1}. The Pearson's linear correlation coefficient between Q_{cell}/m_{cell} and c_{cell} is 0.72. Therefore, as the specific energy of lithium-ion cells increases, the specific heat capacity of the cell is likely to increase as well.

3. Thermal conductivity and resistance

This section reviews thermal conductivity measurements on full-cells, electrode-separator stacks, single stack layers k_l, and thermal contact resistances R_c between theses layers. In comparison to the specific heat capacity, it is not straightforward to formulate an effective thermal conductivity for the entire full-cell with which thermal single-domain models can be parameterized (see Table 1). In the case of pouch cells, the thermal conductivity of the stack [115] can be used with an acceptable uncertainty for full-cells, which is not always the case with prismatic cells [124]. As a result, single-domain models must carefully choose the parameters in this section. In addition, this section does not deal with unspecific conductivities that are used in lumped thermal models [42]. Dry stack layers are also not discussed as complex models are required to determine the wet thermal conductivity from dry measurements [50,72].

The thermal conductivity measurement methods can be divided into steady-state and transient methods. To determine the thermal conductivity, a temperature gradient must be measured that was previously induced by a heat flow. Common steady-state methods in the field of battery cells are the guarded hot plate [34,96] and the comparative method [52,125] with an uncertainty of 2% and 10-20% [43], respectively. Transient methods such as the laser flash achieve uncertainties between 3-5% [43].

Different arrangements of the electrode-separator stack are used for different formats of lithium-ion cells. On the left of Figure 5, a flat-wound arrangement is illustrated, which is usually used for prismatic formats [34,50]. This arrangement represents a combination of the wound and piled stack. Piled stacks are commonly applied for pouch cells [39] and wound stacks for cylindrical cells. To save computational costs, a homogeneous volume often replaces the layered structure of the stack. Due to this layer structure, an anisotropic thermal conductivity must be used for the homogeneous volume, also known as the unit cell [50]. This anisotropy is described by a thermal conductivity in the direction of the stack layers $k_{\parallel}$ and through them $k_{\perp}$. In addition, the coordinate system must be adapted to the stack-arrangement. For example a cylindrical coordinate system (r, z, φ) is recommended for wound stacks and a Cartesian (x, y, z) for piled ones [34].

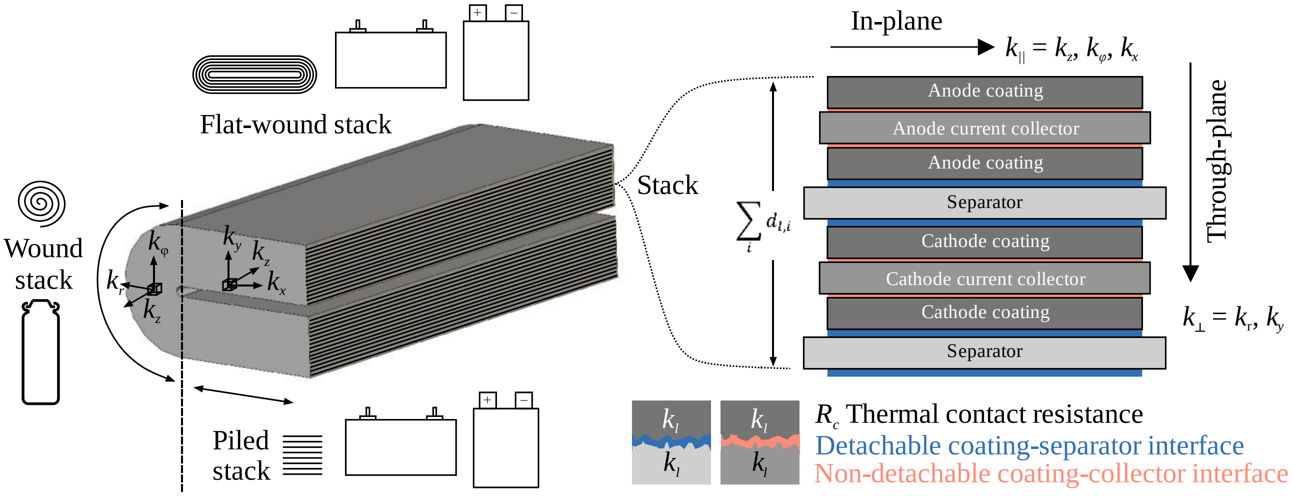

Figure 5: Definition of in-plane $k_\parallel$ and through-plane $k_\perp$ thermal conductivity for wound, piled or flat-wound electrode-separator stacks. The through-plane conductivity of the stack is influenced by the thermal conductivity of the stack layers k_l and the thermal contact resistance R_c between them.

Experiments on the anisotropic thermal conductivity of the stack are reviewed in Subsection 3.1 starting with the in-plane conductivity $k_\parallel$. The in-plane value can be calculated with Equation (9), which is a weighted average of the conductivities of the stack layers k_l by their layer thickness $d_{l,i}$. In contrast, the stack layer with the lowest thermal conductivity and the highest layer thickness dominates the through-plane conductivity $k_\perp$ in Equation (10). Furthermore, $k_\perp$ is affected by thermal contact resistances R_c between the stack layers [126]. R_c can be divided into a detachable coating-separator and a non-detachable coating-collector interface, which are shown in blue and red in Figure 5. It should be noted that R_c is a specific thermal resistance with the unit $\mathrm{cm^2\,K\,W^{-1}}$.

$$k_\parallel = \frac{\sum_i d_{l,i} \cdot k_{l,i}}{\sum_i d_{l,i}} \tag{9}$$

$$k_\perp = \frac{\sum_i d_{l,i}}{\sum R_c + \sum_i \frac{d_{l,i}}{k_{l,i}}} \tag{10}$$

Equations (9) and (10) [126] depend on the layer thicknesses of the electrode-separator stack. For this reason, Table 7 contains exemplary layer thicknesses of lithium-ion cells, which are discussed in the following subsections. For $k_{\parallel}$, the thickness of the anode and cathode current collectors is particularly important (d_{aCC}, d_{cCC}), while for $k_{\perp}$ the layer thicknesses of the separator, anode and cathode coatings (d_{sep}, d_{ano} , d_{cat}) matters the most [34]. In addition, the total stack thickness $\sum_i d_{l,i}$ determines the influence of the thermal contact resistance on $k_{\perp}$.

Table 7: The total thickness of the electrode-separator stack with the thickness shares of the stack layers, which can be used in Equations (9) and (10).

Ref.	$\frac{Q_{cell}}{\text{Ah}}$	Format	Active material	$\frac{\sum_i d_{l,i}}{\text{µm}}$	$\frac{d_{cat}}{\sum_i d_{l,i}}$	$\frac{d_{ano}}{\sum_i d_{l,i}}$	$\frac{d_{aCC}}{\sum_i d_{l,i}}$	$\frac{d_{cCC}}{\sum_i d_{l,i}}$	$\frac{d_{sep}}{\sum_i d_{l,i}}$
[50]	6.8	Prismatic	LCO-G	490	39%	45%	3%	5%	8%
[119]	2.3	Pouch	LCO-G	364	37%	42%	3%	4%	14%
[127]	41.0	Pouch	NMC/LMO-G	350	43%	37%	3%	6%	11%
[101]	14.0	Pouch	LFP-G	223	44%	30%	6%	9%	11%
[78]	8.0	Prismatic	LFP-G	35	26%	11%	17%	17%	29%
[34]	34.0	Prismatic	NMC-G	315	41%	38%	3%	5%	14%
[59]	25.0	Prismatic	NMC-G	357	40%	38%	3%	4%	14%

After discussing the in-plane $k_{\parallel}$ and through-plane $k_{\perp}$ conductivity, Subsections 3.2 and 3.3 examine experimental results on stack layers k_l. Porous components and solid components are treated separately due to the excellent availability of measurement data for solid components such as copper. For this reason, review articles for the solid components already exist, which is why these are only summarized in this paper. Afterwards, the reviewed results for k_l are discussed in relation to $k_{\parallel}$ and $k_{\perp}$ with the help of Equation (9) and (10). For $k_{\perp}$ this includes results for the thermal contact resistance from the last Subsection 3.4.

3.1. Conductivity of electrode-separator stacks and full-cells

Table 8 lists the thermal conductivities measured in in-plane direction $k_{\parallel}$ of the electrode-separator stack or full-cell. Stack conductivities that compensate for the influence of the cell housing in the measurement evaluation are marked with b) in Table 8. These conductivities can be applied directly to the stack in component resolved thermal models or in some cases to single domain models (see Table 1). The stack and full-cell thermal conductivity in the in-plane direction is often viewed as the same for the pouch format with acceptable uncertainty. In the case of prismatic and cylindrical formats, the congruence of the stack and full-cell conductivity depends strongly on the stack and housing geometry. This must be taken into account when using No. 3, 4 and 10 for stacks in component resolved thermal models.

In addition, Q_{cell} and m_{cell} in Table 8 provide information about whether the electrodes are designed for high-energy or high-power applications. The SOH is not included in the header of Table 8 because only Bazinski et al. [128] reported this battery state. It should be noted that in Table 8 only double-coated stacks are taken into account. Therefore, the results of Maleki et al. [29], who only used one separator layer, are not included for reasons of comparability.

LFP and NMC are the most prevalent cathode coatings for in-plane conductivity measurements as can be seen in Figure 2 c). No experiments are available for the cathode coating NCA and the anode coatings LTO. According to the boxplot in Figure 6 a), $k_{\parallel}$ is between 21 and $40.1\,\mathrm{W\,m^{-1}\,K^{-1}}$, which contains all references in Table 8. This represents an uncertainty of ±31% from the mid-range of $30.6\,\mathrm{W\,m^{-1}\,K^{-1}}$. With known cathode and anode chemistry, the uncertainty from the mid-range is reduced to ±21% and ±18% for NMC-G and LFP-G (see Figure 2 c)), respectively. No investigation in Table 8 compares its measurement results with material measurements k_l according to Equation (9). Therefore, Equation (9) has not yet been verified, but is often used in the literature [6,34,54].

The in-plane conductivity shows a weak negative dependency on SOC [128], a negligible influence of the temperature T [59], an unknown relation with SOH, and a negative correlation with the specific capacity Q_{cell}/m_{cell}. Bazinski et al. [128] and Bohn et al. [59] are the only references in Table 8 who examined the dependence on SOC or temperature. Therefore, further experiments are necessary to validate these results. Nevertheless, the experimental results agree with the fact that the in-plane conductivity is strongly influenced by the current collectors [34], which do not change their thickness with the SOC and have minor temperature dependency (Table 10). In addition, the investigation of Bazinski et al. [128] shows a negative correlation between $k_{\parallel}$ and the specific energy or capacity Q_{cell}/m_{cell}. Looking at No. 1 and 2 (Table 8), the specific capacity drops from 37.7 to 28.6 Ah kg^{-1}, while the $k_{\parallel}$ increases from 28.8 to 40.1 W m^{-1} K^{-1}. This is most likely caused by thicker current collectors compared to the total thickness $\sum_i d_{l,i}$ of the stack in Equation (9).

Table 8: Measured thermal conductivity in in-plane direction of the separator-electrode stack or full-cell $k_{\parallel}$. All stacks are soaked with electrolyte (wet) and the measurements were carried out at stack or full-cell level. No information provided is marked with (-).

No.	Ref.	$\frac{Q_{cell}}{\text{Ah}}$	$\frac{m_{cell}}{\text{g}}$	Format	Active material	$\frac{\text{SOC}}{\%}$	$\frac{T}{\text{K}}$	$\frac{k_{\parallel}}{\text{W m}^{-1}\text{ K}^{-1}}$
1	[128]	14.5	385.0	Pouch	LFP-G	50 ±50	305	28.8 ±0.6
2	[128]	10.0	350.0	Pouch	LFP-G	50 ±50	305	40.1 ±1.1
3	[109]	-	-	Cylindr.	LFP-G	100	-	32.0
4	[109]	-	-	Cylindr.	LFP-G	100	-	30.4
5	[90]	25.0	1154.0	Pouch	NMC/LMO-G	-	300	21.0 b)
6	[127]	41.0	-	Pouch	NMC/LMO-G	30	303	25.7 ±0.9
7	[115]	40.0	1180.0	Pouch a)	NMC	-	298	33.0
8	[59]	25.0	-	Prismatic	NMC-G	-	323 ±30	23.1 b)
9	[96]	37.0	-	Prismatic	NMC-G	0	313	21.6 b)
10	[112]	2.6	-	Cylindr.	LCO	-	298	21.9

a) High-energy type. b) The cell housing was compensated for when evaluating the measurement data.

Table 9 contains experimental results for the through-plane conductivity $k_{\perp}$ defined in Figure 5. The header of Table 9 is congruent with Table 8 except of the temperature and SOC dependency $\alpha_{k,T}$ and $\alpha_{k,SOC}$, because more than one dependency is reported for $k_{\perp}$. Both dependencies are determined alike the heat capacity by fitting the reported data with a linear regression. Dividing the slope of the linear regressions $(\partial k_{\perp}/\partial T; \partial k_{\perp}/\partial \text{SOC})$ by the absolute value at 300 K and 50% SOC gives $\alpha_{k,T}$ and $\alpha_{k,SOC}$.

The SOH is not shown in Table 9 because this state was only reported by Bazinski et al. [100], Kovachev et al. [129], Steinhardt et al. [98] and Vertiz et al. [101]. Therefore, future experiments are encouraged to state the SOH of the test cell. Furthermore, measurements are only included in Table 9 if the result is given as a material constant, i.e. it is expressed on specific rather than absolute values. Forgez et al. [42], for example, measured the lumped through-plane (or radial) thermal resistance of a 26650 cylindrical cell. Since they did not convert their absolute resistance between 3.2 and 3.4 K W^{-1} into $k_{\perp}$ with the unit W m^{-1} K^{-1}, the comparison with other geometries is complicated.

Compared to the in-plane conductivity $k_{\parallel}$, the through-plane conductivity $k_{\perp}$ is examined more frequently in the literature. Table 9 lists measurements on 41 different lithium-ion cells, which are analyzed in Figure 2 c) according to cathode chemistry and cell format. Concerning the cathode, LFP is the most abundant chemistry, followed by NMC. Table 9 lists five measurements for which the cathode chemistry is unknown (n/a). In general, as shown in Figure 2 c), all common cathodes are available. It should be noted that most cell measurements do not specify electrode structures (i.e. porosity) and the thickness of the stack layers, which can be a source of uncertainties for the thermal conductivity [130].

NMC-G stacks have a higher thermal conductivity $k_{\perp}$ than LFP-G. This finding is highlighted by the boxplot in Figure 6 a) that determines a median thermal conductivity $k_{\perp}$ for NCA-G, NMC-G and LFP-G of 0.759, 1.034 and 0.404 $\mathrm{W\ m^{-1}\ K^{-1}}$, respectively. The median of all mid-ranges in Table 9 is 0.610 $\mathrm{W\ m^{-1}\ K^{-1}}$ with an outlier of 2.8 $\mathrm{W\ m^{-1}\ K^{-1}}$ (Table 9, No. 40). The mid-range of the whiskers from all measurements is 0.775 $\mathrm{W\ m^{-1}\ K^{-1}}$ with a large uncertainty of ±81%. This uncertainty is reduced for NMC-G (±76%) and LFP-G (±57%) which is approximately twice the uncertainty of the specific heat capacity c_{cell} from Subsection 2.4.

There are only two references (Table 9, No. 10, 32) that report a strong negative correlation of $k_{\perp}$ with SOH. Vertiz et al. [101] observed a decrease in $k_{\perp}$ of -29% between a new and an aged pouch cell (SOH < 80%). The reason for this significant decrease was not discussed by Vertiz et al. [101]. Kovachev et al. [129] cycled three pouch cells at 60°C with different electrical currents (1C to 3C) and pretension between 0 and 0.56 MPa. After 700 cycles, an SOH of 80%, 85% and 86% was reached, which correlated positively with the pretention. The decrease in SOH caused an average decrease in $k_{\perp}$ between 23% and 4% (Figure 6 b)). Kovachev et al. [129] explained the SOH dependence of $k_{\perp}$ with an additional thermal resistance on the anode side caused by the SEI growth. In addition, electrolyte consumption and gas development due to the electrolyte reduction could lead to a decrease in $k_{\perp}$. The results of Vertiz et al. [101] and Kovachev et al. [129] show a significant decrease in $k_{\perp}$ with SOH, which is reflected in a poorer thermal performance of the cell, since the heat development also increases with SOH. However, more research is needed to confirm the correlation between $k_{\perp}$ and SOH for cylindrical and prismatic cells. In addition, further studies with various aging causes such as calendar aging are required.

There are contradictory results regarding the influence of temperature on $k_{\perp}$. As illustrated in Figure 6 b), the temperature dependency $\alpha_{k,T}$ for $k_{\perp}$ lies between -1.5 and +0.1% K^{-1}. Werner et al. [50] and Steinhardt et al. [34,98] explored a dominant decline of $k_{\perp}$ with rising temperature. Murashko [110] et al. confirmed this trend but the intensity of the decline was lesser. No dependency on temperature was explored by Bazinski et al. [100] and a positive trend by Sheng et al. [78,79]. Different results in temperature dependency can be explained by different magnitude of thermal contact resistances R_c, different layer thicknesses or electrode structures. However, the effect of these explanations is not yet fully understood. In addition, no experiments for $k_{\perp}$ are available for safety simulations with temperatures above 340 K.

Table 9: Measured thermal conductivity $k_{\perp}$ in through-plane direction of the separator-electrode stack and full-cells. All stacks are soaked with electrolyte (wet) and the measurements were carried out at stack or full-cell level. No information provided is marked with (-).

No.	Ref.	$\frac{Q_{cell}}{\mathrm{Ah}}$	$\frac{m_{cell}}{\mathrm{g}}$	Format	Active material	$\frac{\mathrm{SOC}}{\%}$	$\frac{T}{\mathrm{K}}$	$\frac{k_{\perp}}{\mathrm{W\,m^{-1}\,K^{-1}}}$	$\frac{\alpha_{k,T}^{a)}}{\%\,\mathrm{K}^{-1}}$	$\frac{\alpha_{k,SOC}^{b)}}{\%}$
1	[131]	2.3	70.0	Cylindr.	LFP-G	-	296	0.510	-	-
2	[109]	-		Cylindr.	LFP-G	100	286	0.150	-	-
3	[109]	-		Cylindr.	LFP-G	100	286	0.200	-	-
4	[45]	4.4	194.0	Cylindr.	LFP-G $^{g)}$	50	303	0.350$^{i)}$	-	-
5	[110]	2.5	70.0	Cylindr.	LFP-G	50 ±50	314 ±19	0.472 ±0.03	-0.2	-4
6	[132]	2.3	-	Cylindr.	LFP	-	-	0.200	-	-
7	[108]	2.5	70	Cylindr.	LFP-G $^{g)}$	50 ±50	-	0.458 ±0.01	-	-5
8	[100]	14.0	385.0	Pouch $^{d)}$	LFP-G	50 ±50	298 ±30	0.350 ±0.01	0.0	-5
9	[78]	9.0	235.0	Pouch $^{e)}$	LFP-G	50	293 ±40	0.522 ±0.02	0.1	-
10	[101]	14.0	-	Pouch	LFP-G	50 ±50	-	0.242 ±0.04	-	-4$^{c)}$
11	[78]	8.0	328.0	Prismatic $^{e)}$	LFP-G	50 ±50	293 ±40	0.540 ±0.02	0.1	-3
12	[124]	60	2000	Prismatic	LFP-G	-	-	0.485	-	-
13	[50]	6.8	150.0	Prismatic	LCO-G	70	318 ±15	0.821$^{i)}$±0.16	-1.1	-
14	[105]	2.1	45.0	Cylindr.	LCO-G	50	298	0.239	-	-
15	[112]	2.6	-	Cylindr.	LCO	-	298	0.385 ±0.17	-	-
16	[100]	75.0	-	Pouch $^{d)}$	NMC-G	50 ±50	298	0.430 ±0.01	-	-7
17	[78]	9.0	222.0	Pouch $^{e)}$	NMC-G	50	293 ±40	0.629 ±0.02	0.1	-
18	[115]	40.0	1180.0	Pouch $^{f)}$	NMC $^{h)}$	-	298	0.610	-	-
19	[34]	34.0	-	Prismatic	NMC-G	15	293 ±22	1.100$^{i)}$±0.40	-1.5	-
20	[38]	43.0	840.0	Prismatic	NMC $^{h)}$	50	298	0.820	-	-

21	[59]	25.0	-	Prismatic	NMC-G	-	323 ±30	1.100	0.0	-
22	[96]	37.0	-	Prismatic	NMC-G	0	308	1.034 i)	-	-
23	[105]	3.5	49.0	Cylindr.	NMC-G	50	298	0.186	-	-
24	[79]	2.4	44.7	Cylindr.	NMC-G	-	293 ±40	1.041 ±0.04	0.1	-
25	[79]	4.6	65.9	Cylindr.	NMC-G	-	293 ±40	1.164 ±0.03	0.1	-
26	[98]	3.4	49.0	Cylindr.	NMC-SiG	40 ±30	300 ±15	1.250 i) ±0.14	-0.5	10
27	[98]	4.8	69.0	Cylindr.	NMC-SiG	43 ±28	300 ±15	1.352 i) ±0.21	-0.7	12
28	[108]	4.4	82	Cylindr.	NMC-G h)	50 ±50	-	0.540 ±0.02	-	-7
29	[87]	-	-	Pouch	LMO-LTO g)	50 ±40	298	0.641 ±0.05	-	-6 c)
30	[90]	25.0	1154.0	Pouch	NMC/LMO-G	-	300	0.480 i)	-	-
31	[127]	41.0	-	Pouch	NMC/LMO-G	30	290	0.780 ±0.06	-	-
32	[129]	41.0	-	Pouch	NMC/LMO-G	50 ±50	-	0.675 ±0.13	-	7 c)
33	[110]	2.7	48.0	Cylindr.	NCA-G	50 ±50	314 ±19	0.786 ±0.13	-0.2	24
34	[105]	3.6	48.0	Cylindr.	NCA-G	50	298	0.413	-	-
35	[108]	2.7	48.5	Cylindr.	NCA-G h)	50 ±50	-	0.763 ±0.10	-	25
36	[108]	3.1	48.5	Cylindr.	NCA-SiG h)	50 ±50	-	0.754 ±0.12	-	33
37	[102]	-	-	Cylindr.	-	-	-	0.390	-	-
38	[47]	1.8	42.7	Cylindr.	-	100	296	0.900 i)	-	-
39	[47]	1.5	39.5	Cylindr.	-	100	296	1.400 i)	-	-
40	[47]	1.3	41.6	Cylindr.	-	100	296	2.800 i)	-	-
41	[47]	1.4	40.9	Cylindr.	-	100	296	1.200 i)	-	-

a) The temperature dependency $\alpha_{k,T}$ is determined by dividing the slope of the linear regression $\partial k_{\perp}/\partial T$ by the thermal conductivity at 300 K $k_{\perp}(300\text{K})$. b) The SOC dependency $\alpha_{k,SOC}$ is determined by dividing the slope of the linear regression $\partial k_{\perp}/\partial \text{SOC}$ by the thermal conductivity at a SOC of 50%. c) Nonlinear relation between SOC and $k_{\perp}$ reported. d) Applied compression load 1500 N. e) Vacuum environment. f) Atmospheric pressure. g) High-power type. h) High-energy type. i) The cell housing was compensated for when evaluating the measurement data.

As illustrated in Figure 6 b), the SOC dependency $\alpha_{k,SOC}$ implies a change in $k_{\perp}$ between -7% and +33% when the SOC is increased from 0% to 100%. It should be noted that $\alpha_{k,SOC}$ assumes a linear relationship between SOC and $k_{\perp}$ and three references measured a parabolic relationship (Table 9, No.10, 29, 32). For example, Vertiz et al. [101] observed a reduction in thermal conductivity of -17.22% and -16.23% at a full-cell SOC of 0% and 100%, respectively, compared to the thermal conductivity at 50% SOC. In contrast, the remaining five references in Table 9 are well described by a linear relationship.

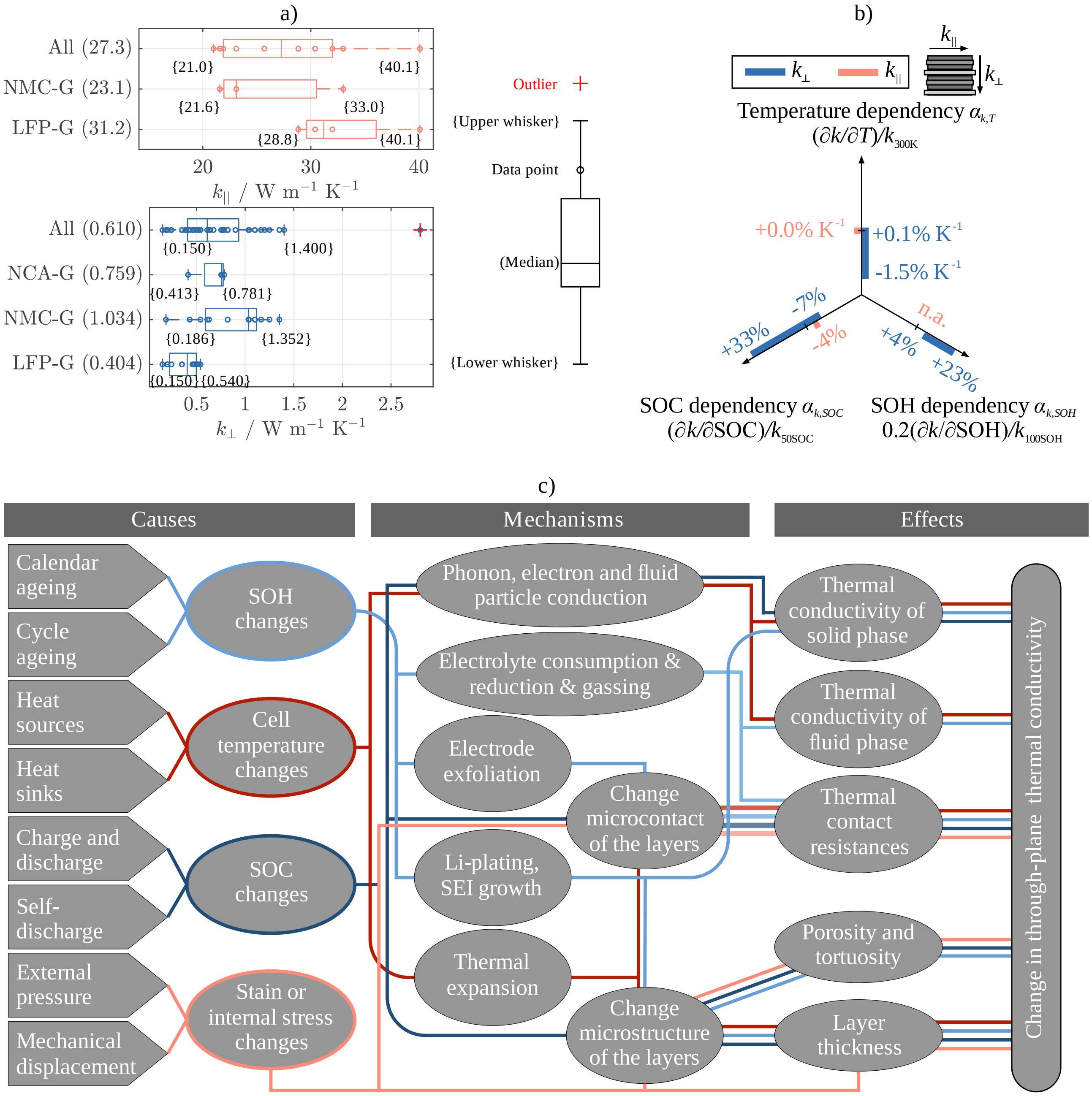

Figure 6: Range of values and dependencies of the in-plane $k_{\|}$ and through-plane $k_{\perp}$ conductivity of the electrode-separator stack and full-cells. a) Boxplot of the mid-range conductivities listed in Table 8 and Table 9. Round brackets indicate recommended values (medians) for thermal modeling. b) Dependencies on cell temperature, SOC, and SOH. c) Schematic of causes, mechanisms and effects for changes in thermal conductivity $k_{\perp}$ in through-plane direction.

The dependence of $k_\perp$ on the SOC is often explained by a changing thermal conductivity of the active particle with the degree of lithiation [78,87,110]. This explanation is supported by the work of Ju et al. [133] and Cho et al. [134], who reported a strong correlation between the thermal conductivity of graphite and LCO with the degree of lithiation. For example, Cho et al. [134] measured a decrease in thermal conductivity from 5.4 to 3.7 $\mathrm{W\,m^{-1}\,K^{-1}}$ during the delithiation from $Li_{1.0}CoO_2$ to $Li_{0.6}CoO_2$. A strong dependence of $\alpha_{k,SOC}$ on the cathode material also explains the opposite dependence of -4% and + 33% for an LFP and NCA cell, which were measured using the same test method (Table 11, No. 5, 33). However, such a strong dependence on the cathode material was not explored by Bazinski et al. [100]. Further measurements are therefore required to clarify whether a linear or non-linear relationship between $k_\perp$ and SOC exist and which cell parameters influence this relationship.

Instead of measuring, the through-plane conductivity can be calculated with Equation (10) if the layer thickness d_l and the layer conductivity k_l are known. The validity of this calculation depends on the thermal contact resistance R_c, which is not a material-specific property. Some of the references in Table 9 determined $k_\perp$ with Equation (10) neglecting R_c. Vertiz et al. [101] and Sheng et al. [78] overestimated $k_\perp$ in their calculation by 255% and 59%, respectively. Both authors explained this overestimation with thermal contact resistances between the stack layers, but uncertainties in the selected layer conductivities k_l could also be an explanation. Uncertainties arising from k_l can be neglected for the calculation of Werner et al. [50], because they used an LCO cell whose k_l was previously measured by Loges et al. [130]. They achieve an excellent agreement between their experiments and calculations, which confirms the assumption that R_c can be neglected. However, more research is needed to understand the relevance of R_c to $k_\perp$.

Variabilities in $k_\perp$of lithium-ion cells are practically always ignored in thermal models. However, as discussed in this paper, several studies in the literature have shown that changes in SOC, SOH and temperatures can lead to variations in $k_\perp$. One of the remaining challenges is that the causes of these effects on $k_\perp$ are multifaceted in nature, and so far, the causal relationships have been barely investigated. The complexity of the cause-effect chain is illustrated in Figure 6 c) for $k_\perp$ using a network graph. For the interest of the reader, we provide a visual summary of the main causes and effects, and the mechanisms by which they can be mediated. Note that this network graph is not intended to illustrate every cause, mechanism or effect.

In Figure 6 c), we have divided the cause-effect chain for $k_\perp$ into causes, mechanisms and effects. The primary causes are fundamental processes related with battery operation, i.e. heat transfer, ageing, mechanical, and charge/discharge processes. These are directly linked to the secondary causes, which are changes in key battery states, such as temperature, SOH, SOC, strain or internal stress. Then these changes in battery states are linked to seven underlying mechanisms leading to five primary effects considered in Equation (10) and porous media theory such as Krischer [50]. For example, 1) a change in thermal conductivity in the liquid phase could result from electrolyte consumption [129] if the electrolyte is replaced by gases with low thermal conductivity. 2) The thermal conductivity of the solid phase depends on the phonon and electron conduction, which are influenced by the crystal lattice parameters [133]. 3) Changes in porosity or tortuosity can influence the weighting between solid and fluid phase and thus the overall through-plane conductivity. 4) According to Equation (10), thermal contact resistances due to nanoscopic contact points must be taken into account for heat conduction. 5) The change in thickness of the stacked layers due to mechanical stresses within the cell or changes in the microstructure could further influence $k_\perp$.

The line colors in Figure 6 c) illustrate the cause-effect chain of the individual battery states such as SOH, temperature, SOC or internal mechanical stress. An increase in the stress can, for example, change the microcontacts between the stacked layers [135], which is known to affect the thermal contact resistance. The temperature can influence the thermal conduction by phonons [136] and thus the thermal conductivity of every solid phase within the cell. In addition, the thermal expansion influences the microcontact and the microstructure of the cell layers, which both have effects on $k_\perp$. SOC can change $k_\perp$ through several mechanisms, which are also triggered by temperature or mechanical stress within the cell. Further mechanisms must be taken into account for the battery state SOH. For example, Li-plating or SEI growth changes the composition of the solid phase and the porosity [15] , which can affect the overall $k_\perp$. In addition, mechanisms such as electrode exfoliation [137] should have a strong influence on the thermal contact resistance. Overall, Figure 6 c) shows that the discussion of the relationship between battery states and $k_{\perp}$ is not trivial and further experimental and modeling efforts are required in order to understand the cause-effect chain.

3.2. *Conductivity of solid non-porous components*

As discussed in Subsection 2.2, lithium-ion cells contain solid non-porous components such as the current collectors, whose dimensions and design may influence the thermal conductivities of the stack, as thoroughly discussed for a cylindrical cell by Li et al. [36]. In addition, thermal models require the thermal conductivity of all subcomponents of the cell housing (see Figure 1), which are solid too. Table 10 lists the thermal conductivity and temperature dependence $\alpha_{k,T}$ of important solid materials that are often used for the stack or the cell housing.

Most of the thermal conductivities in Table 10 are recommended thermal conductivities based on a variety of measurements in the literature. For example, the thermal conductivity of stainless steel from Bogaard et al. [138] is based on 15 different thermal conductivity measurements. Therefore, the thermal conductivity in Table 10 already has a strong data integrity, which is why a comparison of different investigations is dispensed with.

Copper and aluminum show a slight temperature dependence $\alpha_{k,T}$, but a significant dependence on the composition. According to Equation (9), the in-plane thermal conductivity is strongly influenced by the current collectors made of copper and aluminum. Therefore, the small magnitude of $\alpha_{k,T}$ of copper and aluminum explains the temperature dependence of $k_{\parallel}$ in Figure 6 b), which is also close to zero. In addition to the temperature, the composition is also a dominant factor for thermal conductivity. This can be seen when comparing pure aluminum with the alloy 3003. Due to the 1.1% manganese composition of this alloy, the thermal conductivity drops by -35% from 237.5 to $155\,\mathrm{W\,m^{-1}\,K^{-1}}$. The strong dependency on the composition is also observed with stainless steel [138]. Therefore, the composition of each component of the cell must be carefully identified for accurate thermal cell models.

Table 10: Measured thermal conductivity of solid non-porous components in lithium-ion cells. No information provided is marked with (-).

Material	$\frac{T}{\mathrm{K}}$	$\frac{k_s}{\mathrm{W\ m^{-1}\ K^{-1}}}$	$\frac{\alpha_{k,T}^{\mathrm{f)}}}{\mathrm{\%\ K^{-1}}}$
Copper a)	300 ±50 [139]	399.0 ±5.0 [139]	-0.0
Aluminum b)	300 ±50 [139]	237.5 ±2.5 [139]	+0.0
Aluminum alloy 3003 c)	-	155 [89]	-
PP d)	273 ±50 [67]	0.215 ±0.01 [67]	0.0 g)
PET d)	301 ±25 [140]	0.188 ±0.00 [140]	0.0
PE d)	313 ±40 [141]	0.241 ±0.02 [141]	-0.2 g)
Stainless steel AISI 304 e)	300 ±50 [138]	14.850 ±0.86 [138]	+0.1
Pouch foil [37]	-	55.1 (‖) , 0.269 (⊥)	-

a) Anode current collector, Negative cell terminal. b) Cathode current collector, Anode current collector (LTO)[87], Positive cell terminal. c) Prismatic cell housing [34,77,78], Cylindrical housing [45]. d) Pouch foil layer, separator. e) Cylindrical housing [79,88], Prismatic cell housing [50], Cylindrical mandrel / center pin [80]. f) The temperature dependency $\alpha_{k,T}$ is determined by dividing the slope of the linear regression $\partial k/\partial T$ by the termal conductivity at 300 K. g) Nonlinear relation between T and k.

The thermal conductivity of pouch foils has a pronounced anisotropic thermal conductivity, which results from the aluminum and polymer layers discussed in Subsection 2.2. Yi et al. [37] measured the thermal conductivity of a pouch foil used in a commercial cell from LG Chem Ltd.. Their measurement results are listed in Table 10, which have a similar thermal conductivity for the in-plane (‖) and through-plan (⊥) directions as discussed for the electrode-separator stack in Subsection 3.1. The result of Yi et al. [37] corresponds to theoretical calculations such as those carried out by Rheinfeld et al. [21], which resulted in a thermal conductivity in in-plane (‖) and through-plan (⊥) direction of 67.08 and 0.25 $\mathrm{W\ m^{-1}\ K^{-1}}$, respectively. The influence of the pouch foil on the through-plane conductivity of the stack $k_{\perp}$ should be small due to the low ratio between foil thickness and total cell thickness of 4% to 5% [21,37] and the similarity of the through-plane conductivity of the stack and pouch film.

3.3. *Conductivity of porous components*

This subsection deals with the thermal conductivity of porous stack layers, which can be used in Equation (9) and (10) to calculate $k_{\perp}$ and $k_{\|}$. Since the pores of an operational lithium-ion cell contain electrolyte, only wet layer conductivities k_l are discussed below. Dry layers are omitted in this subsection, as at least the porosity and tortuosity must be known [50] in order to calculate the wet conductivity, which is often not the case. This is different from heat capacity, where dry measurements are more useful.

Table 11 lists wet conductivities k_l for various separators, anode and cathode coatings used in the electrode-separator stack in Figure 5. Most of the references in Table 11 give the temperature T, which has a median of 296 K. The SOC and SOH of the full-cell are not included in the header of Table 11 as they are rarely stated in the references, in part because materials such as the separator do not store charge. The compression pressure p is included in Table 11 due to its expected influence on k_l [52].

According to Figure 2 d), all common stack layers in lithium-ion cells have been measured except of LMO, NCA, silicon-graphite and LTO. Despite the importance of LFP, there is only one experiment for this cathode coating (Table 11, No. 28). Therefore, more k_l measurements are required for LFP to increase integrity and determine uncertainties. It should also be mentioned that the porosity ϵ is rarely given despite its high effect on k_l. Only Yang et al. [53] and Liebig et al. [58] state the porosity of their stack layers. Therefore, it is recommended to indicate the porosity in future investigations.

Table 11: Measured thermal conductivity of porous stack layers k_l applied in electrode-separator stacks of lithium-ion cells. All stack layers are soaked with electrolyte (wet) and contain no collector foils or substrate. No information provided is marked with (-).

No.	Ref.	Stack layer	$\frac{T}{\mathrm{K}}$	$\frac{p}{\mathrm{bar}}$	$\frac{k_l}{\mathrm{W\ m^{-1}\ K^{-1}}}$
1	[52]	NMC	296	6.9 ±4.6	0.895 ±0.02
2	[135]	NMC	-	-	0.830
3	[58]	NMC (ϵ = 0.191)	298	-	0.660
4	[125]	NMC (Pristine)	296	6.9 ±4.6	0.550 ±0.01
5	[125]	NMC (Aged)	296	6.9 ±4.6	0.540 ±0.02
6	[52]	Separator (PET, Al_2O_3)	296	6.9 ±4.6	0.375 ±0.02
7	[52]	Separator (PET, Al_2O_3)	296	6.9 ±4.6	0.380 ±0.02
8	[52]	Separator (PET, Al_2O_3)	296	6.9 ±4.6	0.335 ±0.02
9	[52]	Separator (PET, Al_2O_3)	296	6.9 ±4.6	0.290 ±0.01
10	[52]	Separator (PP, Al_2O_3)	296	6.9 ±4.6	0.120 ±0.02
11	[52]	Separator (glass microfiber)	296	6.9 ±4.6	0.190 ±0.01
12	[52]	Separator (No. 13 without $LiPF_6$)	296	6.9 ±4.6	0.220 ±0.01
13	[52]	Separator	296	6.9 ±4.6	0.230 ±0.01
14	[54]	Separator (PP)	-	-	0.334
15	[53]	Separator (PP, PE)	-	-	0.190
16	[53]	Separator (PVDF-HFP [a)], Al_2O_3)	-	-	0.920 ±0.21
17	[58]	Separator (ϵ = 0.395)	298	-	0.680
18	[52]	Graphite	296	6.9 ±4.6	1.270 ±0.16
19	[52]	Graphite	296	6.9 ±4.6	1.130 ±0.24

20	[52]	Graphite	296	6.9 ±4.6	1.450 ±0.27
21	[142]	Graphite	295	9.3	0.890
22	[142]	Graphite	295	9.3	0.360
23	[142]	Graphite	295	9.3	1.260
24	[58]	Graphite (ϵ = 0.308)	298	-	1.450
25	[135]	Graphite	-	-	1.440
26	[125]	Graphite (Pristine)	296	6.9 ±4.6	0.685 ±0.02
27	[125]	Graphite (Aged)	296	6.9 ±4.6	0.615 ±0.02
28	[52]	LFP	296	6.9 ±4.6	0.340 ±0.02
29	[54]	LCO	-	-	1.580
30	[142]	LCO	295	9.3	1.100

a) Hexafluoropropylene

Figure 7 a) displays the medians and whiskers of the mid-ranges of k_l in Table 11. According to this boxplot, separators have a median conductivity of $0.312\ \mathrm{W\ m^{-1}\ K^{-1}}$ with two identified outliers (Table 11, No. 16, 25). The whiskers and the mid-range of $0.25\ \mathrm{W\ m^{-1}\ K^{-1}}$ determine the uncertainty of ±52%. Separators in lithium-ion cells are usually made of PET, PE or PP [52], materials with a thermal conductivity below $0.25\ \mathrm{W\ m^{-1}\ K^{-1}}$ as shown in Table 10. Considering that the thermal conductivity of common electrolytes is below $0.2\ \mathrm{W\ m^{-1}\ K^{-1}}$ [50,143], the median of $0.312\ \mathrm{W\ m^{-1}\ K^{-1}}$ is inconsistent. The inconsistency could be explained by the presence of Al_2O_3 ($35\ \mathrm{W\ m^{-1}\ K^{-1}}$ [53]) ceramic particles or coatings, which are used in composite separators to provide pathways for efficient heat transfer [53] and to increase safety [144]. Parikh et al. [145] showed, for example, that the ceramic coatings can increase the thermal conductivity of the separator from 0.2 to $0.6\ \mathrm{W\ m^{-1}K^{-1}}$, which could explain the outliers in Figure 7 a). Consequently, the volume of Al_2O_3 particles inside the separator has to be taken into account for the thermal conductivity of the separator, which is rarely the case.

According to the median in Figure 7 a), wet graphite layers have a thermal conductivity of $1.195\ \mathrm{W\ m^{-1}\ K^{-1}}$ with an uncertainty of ±60% based on the mid-range of $0.905\ \mathrm{W\ m^{-1}\ K^{-1}}$. The large uncertainty is mainly caused by the lower whisker of $0.360\ \mathrm{W\ m^{-1}\ K^{-1}}$ (Table 11, No. 22). This anode coating was an in-house carbon material that was not graphitized by heat treatments [142]. Therefore, when choosing the right k_l for the anode coating, the heat treatment must also be considered.

According to the box plot in Figure 7 a), LCO has the highest cathode thermal conductivity followed by NMC and LFP. Yang et al. [146] explained the relationship between LCO and NMC using phonon transport. According to their calculation, the thermal conductivity of NMC decreases with decreasing Co content, which means that LCO has a higher thermal conductivity than NMC111 and NMC111 a higher conductivity than NMC 811. The uncertainties for LCO and NMC in Figure 7 a) are ±18% and ±25%, respectively. The higher uncertainty of NMC could be caused by different Co contents. Nevertheless, cathode coatings show less uncertainty than graphite coatings.

The temperature dependency $\alpha_{k,T}$ of wet k_l has been poorly investigated in the literature. Only Liebig et al. [58] measured $\alpha_{k,T}$ for a wet graphite, NMC and separator coating and observed an increase in thermal conductivity with increasing temperature. This positive correlation of k_l with T contradicts some of the findings for $k_\perp$ in the literature [34,50], which is why Liebig et al. [58] questioned the transferability of their results to other battery models. This underscores the need for further research on the temperature dependence of wet k_l.

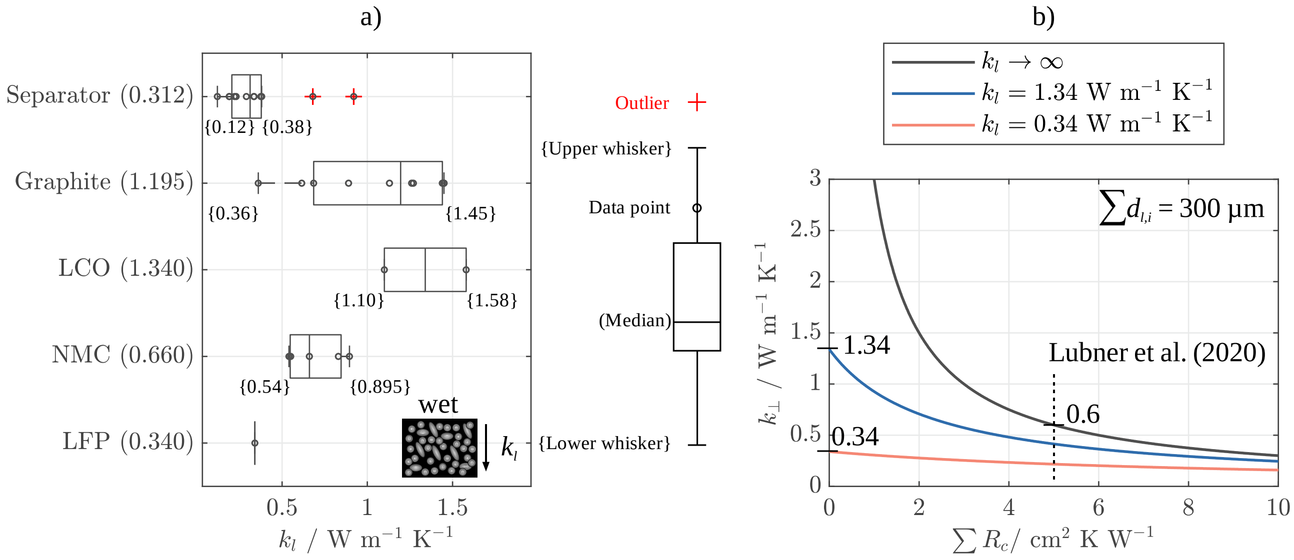

Figure 7: The thermal conductivity of wet stack layers k_l and the thermal contact resistance R_c, which determine the through-plane conductivity $k_\perp$ of the electrode-separator stack according to Equation (10). a) Boxplot for k_l from Table 11 with recommended (median) conductivities for thermal modeling, indicated by round brackets. b) Dependence of $k_\perp$ on the sum of the thermal contact resistances $\sum R_c$ for a stack thickness of 300 µm and a constant k_l specified in the legend for each stacking layer.

The relationship between the degree of lithiation and the thermal conductivity of wet anode and cathode coatings has not yet been measured. Only dry measurement are available in the literature. For example, Gotcu et al. [57] increased the degree of lithiation of dry NMC and LCO coatings from 0 and 1, which in turn increased the thermal conductivity for both coatings by more than 32%. This finding would indicate a negative correlation between the SOC of the full cell and $k_\perp$ if the graphite conductivity is independent of the SOC. There are neither wet nor dry thermal conductivity measurements for graphite coatings with different degrees of lithiation in the literature. However, molecular dynamics simulations show a strong increase in the graphite thermal conductivity with increasing lithiation [133], which was reasoned by the change in sound velocity with lithiation. This would suggest a positive correlation between the SOC of the full-cell and $k_\perp$. In summary, there are arguments for a positive and arguments for a negative correlation between SOC and $k_\perp$, which is consistent with Figure 6 b).

According to the study by Richter et al. [52], the thermal conductivity of the wet anode and cathode coatings increases with increasing pressure p, while no significant correlation was measured for the separator. The pressure dependency could be caused either by thermal contact resistances during the measurement or by changing porosity of the active material [147]. The pressure dependence of k_l could explain a correlation between SOC and $k_\perp$ if the pressure in the stack is influenced by the SOC. In addition, Richter et al. [125] examined the effects of different SOH on the thermal conductivity of k_l and found no significant changes with aging. This contradicts Vertiz et al. [101] and Kovachev et al. [129], who measured a sharp drop in $k_\perp$ with aging (Table 9, No. 10, 32). Therefore, more research is needed to clarify this inconsistency.

3.4. Contact resistances

Any heat that flows through a solid-solid [148] or solid-liquid [149] interface must overcome thermal contact resistance in the unit $\mathrm{cm}^2\ \mathrm{K}\ \mathrm{W}^{-1}$. This resistance arises due to the narrowing of the heat flow at the nanoscopic contacts at the interface and the acoustic mismatch between dissimilar materials [135,150]. The thermal contact resistance appears on every length scale of lithium-ion cells. On the nanoscale, intra-grain thermal resistances in active particles such as LCO can reduce the thermal conductivity of the monocrystalline material [151]. In the micrometer scale, there is solid-solid contact resistance between the particles and the binder and solid-liquid contact resistance between the solid phase and the electrolyte. This subsection deals with the macroscale thermal contact resistance within the layer structure of lithium-ion cells (see Figure 5).

On the macro scale, the thermal contact resistance results from a parallel connection of the resistance caused by the interstitial material and the series connection of the two resistors due to the phonon mismatch and the constriction of the heat flow [135]. Increasing the thermal conductivity of the electrolyte and increasing the particle radius and pressure can therefore reduce the overall contact resistance [135]. In addition, reducing porosity and improving adhesion between the stacked layers can reduce contact thermal resistance [152]. For example, surfactants could be used to control particle size and porosity [153].

There are two types of thermal contact resistance on the macro scale. The first type (R_c) takes into account the interfaces between the stack layers, which are marked in blue and red in Figure 5. Therefore, this contact resistance occurs several times from the core to the shell of the cell. The second type appears only once, namely between the cell housing and the electrode-separator stack. Gaitonde et al. [154] investigated the second type, which is usually an interface between the separator and the housing. They measured an inverse contact resistance of $670\,\mathrm{W\,m^{-2}\,K^{-1}}$ with no significant dependence on pressure or temperature. Gaitonde et al. [154] regarded their results as an upper limit, since the separator was not saturated with electrolyte and the contact resistance generally decreases with liquid interstitial materials [155]. Therefore, further investigations into the thermal contact resistance of the interface between separator and cell housing with electrolyte as interstitial material are warranted.

The thermal contact resistance between the stacked layers was further subdivided into a non-detachable coating-collector interface and a detachable coating-separator interface in Figure 5. The contact resistance of the coating-collector interface is often neglected [152], probably because of the calendaring during electrode production, but there is no experimental evidence to support this assumption in the literature. Comparable interfaces such as thermally conductive adhesives on aluminum generate a thermal contact resistance between 0.07 and $0.3\,\mathrm{cm^2K\,W^{-1}}$ [156]. For the entire stack in Figure 5, this would mean a contribution of 0.28 to $1.2\,\mathrm{cm^2 K\,W^{-1}}$ to the total thermal contact resistance $\sum R_c$ in Equation (10).

In Subsection 3.1, it was mentioned that the measured through-plane conductivity $k_\perp$ of the stack is lower than the calculated value for $k_\perp$ if the contact resistances are neglected ($\sum R_c = 0$). A total thermal contact resistance between the stack layers $\sum R_c$ of 0.24 and $12.98\,\mathrm{cm^2 K\,W^{-1}}$ could explain the discrepancy between the calculated and measured conductivity $k_\perp$. The range between 0.24 and $12.98\,\mathrm{cm^2 K\,W^{-1}}$ is described in Table 12 for the experiments conducted by Sheng et al. [78] and Vertiz et al. [101]. To estimate $\sum R_c$, the calculated and measured thermal resistance $(\sum_i d_{l,i})/k_\perp$ of the stack is first determined. The difference between these two resistances gives the estimated thermal contact resistance $\sum R_c$ of 0.24 and $12.98\,\mathrm{cm^2\ K\,W^{-1}}$. The large variation of the $\sum R_c$ underlines the need for further $k_\perp$ experiments which specify the thicknesses and materials of the stacked layers.

Table 12: Estimation of the thermal contact resistance between the stack layers $\sum R_c$ based on thermal conductivity measurements $k_\perp$ in Table 9 (No. 11, 10).

	Sheng et al. [78]	Vertiz et al. [101]	Unit
Calculated $k_\perp$	0.86	1.01	$\mathrm{W\,m^{-1}K^{-1}}$
Measured $k_\perp$	0.54	0.242	$\mathrm{W\,m^{-1}K^{-1}}$
Stack thickness $\sum_i d_{l,i}$	35	413	µm
Calculated $(\sum_i d_{l,i})/k_\perp$	0.41	4.09	$\mathrm{cm^2\ K\,W^{-1}}$
Measured $(\sum_i d_{l,i})/k_\perp$	0.65	17.07	$\mathrm{cm^2\ K\,W^{-1}}$
Estimated $\sum R_c$	0.24	12.98	$\mathrm{cm^2\ K\,W^{-1}}$

The estimates for $\sum R_c$ in Table 12 can be compared with measurement results for $\sum R_c$ in Table 13. All measurement results listed in Table 13 were carried out on stack layers that were either extracted from full-cells or produced in-house. Table 13 also provides information about the interstitial material (dry/wet), the apparent pressure p during the test, the temperature, and the non-detachable interfaces that are included in the measured contact resistance R_c. If R_c can be used to calculate the total contact resistance $\sum R_c$ of the electrode-separator stack, it is also listed in Table 13. For example, No. 9 includes a separator-NMC and a separator-graphite interface. Since both interfaces appear twice in stacks (Figure 5), R_c is multiplied by two for the total contact resistance $\sum R_c$. By this measure, the results in Table 13 can be used in Equation (10) to calculate $k_\perp$.

Lubner et al. [135] measured a total contact resistance $\sum R_c$ of $4.94\ \mathrm{cm}^2\ \mathrm{W}\ \mathrm{K}^{-1}$. They investigated R_c with stationary *ex-situ* and transient *in-situ* measurements. For the *ex-situ* measurement, they clamped graphite and NMC electrodes between two copper rods and measured the contact resistance (Table 13, No 4-7) with and without electrolyte. It can be seen that the use of electrolyte as the interstitial material (wet) reduces the contact resistance by more than 66% compared to the dry resistance. In addition, wet R_c of the graphite-copper interface is of the same order of magnitude as the cathode-separator interface. This contradicts Vishwakarma et al. [152] who neglected the thermal contact resistance of graphite interfaces. For the *in-situ* measurement, Lubner et al. [135] implemented eight omega-3 thermal conductivity sensors in a single-layer pouch cell. During the formation cycles, they arrived at a contact resistance of $2.47\ \mathrm{cm}^2\ \mathrm{W}\ \mathrm{K}^{-1}$ for an external compaction pressure of 0.34 bar. They assigned this contact resistance to a single anode-separator and cathode-separator interface. Therefore, for double-coated electrode-separator stacks, this would lead to a total contact resistance $\sum R_c$ of $4.94\ \mathrm{cm}^2\ \mathrm{W}\ \mathrm{K}^{-1}$, which is in the estimated range in Table 12.

Vishwakarma et al. [152] claimed that 88% of the stack's thermal resistance is determined by the cathode-separator interface. They explained the dominance of the cathode-separator interface by a larger mismatch in phonon speed compared to the anode-separator interface. Vishwakarma et al. [152] carried out three stationary conductivity measurements with the same setup as Lubner et al. [135] on dry separator and cathode electrodes. Like Lubner et al. [135], they had to compensate for the resistance of the electrode material. For this compensation, they neglected effects of the electrolyte to the heat transport, which completely contradicts the literature [52,125,142] and overestimates the contact resistance. This likely overestimated and dry contact resistance results in an $8.4\ \mathrm{cm}^2\ \mathrm{W}\ \mathrm{K}^{-1}$ for the entire stack. In addition, Vishwakarma et al. [152] made some surface modifications to the cathode and separator that reduced the $\sum R_c$ to $1.8\ \mathrm{cm}^2\ \mathrm{W}\ \mathrm{K}^{-1}$.

One of the first R_c measurements was carried out by Ponnappan et al. [155] with a similar test setup as used by Vishwakarma et al. [152] and Lubner et al. [135]. According to the description of the experiment, the resistance of the material $(\sum_i d_{l,i})/k_\perp$ was not subtracted from R_c. Therefore, the R_c stated by Ponnappan et al. [155] includes the contact resistance and the resistance of the material. The R_c of the wet stack (Table 13, No. 1) shows a slight dependence on temperature and pressure. However, due to the detachable Cu-coating interfaces, the results cannot be used directly for $\sum R_c$. The result of Ponnappan et al. [155] of 3.48 $\mathrm{cm}^2\ \mathrm{W\ K}^{-1}$ can be subtracted by the wet Cu interfaces of Lubner et al. [135] (Table 13, No. 2 and 3), which gives a compensated R_c of 1.54 $\mathrm{cm}^2\ \mathrm{W\ K}^{-1}$. This compensated R_c would result in a total contact resistance $\sum R_c$ of 3.08 $\mathrm{cm}^2\ \mathrm{W\ K}^{-1}$.

Smaller thermal contact resistances, as reported by Lubner et al. [135], are consistent with the literature. Figure 7 b) shows the through-plane conductivity $k_\perp$as a function of the thermal contact resistances $\sum R_c$ with three different values for the stack layers k_l according to Equation (10). The lower value for k_l of 0.34 $\mathrm{W\ m}^{-1}\ \mathrm{K}^{-1}$ is chosen according to the median of wet LFP coating in Figure 7 a) and 1.34 $\mathrm{W\ m}^{-1}\ \mathrm{K}^{-1}$ according to LCO. The black line ($k_l \to \infty$) represents the maximum $k_\perp$ for a given value of $\sum R_c$. For $\sum R_c$ of Lubner et al. [135] in Table 13, the black line indicates a maximum of 0.6 $\mathrm{W\ m}^{-1}\ \mathrm{K}^{-1}$ for a stack thickness of 300 µm, which is below the maximum of 1.4 $\mathrm{W\ m}^{-1}\ \mathrm{K}^{-1}$ in Table 9 measured for $k_\perp$. Therefore, smaller thermal contact resistances as reported by Lubner et al. [135] are possible. Figure 7 b) shows that thermal contact resistances $\sum R_c$ and the thermal conductivity of the stack layers k_l equally influence $k_\perp$, which makes their separation difficult.

Table 13: Measured thermal contact resistances R_c for interfaces within the electrode-separator stack in lithium-ion cells. If R_c can be used in Equation (10) to calculated $k_\perp$, it is cumulated adequately for the total thermal contact resistance $\sum R_c$ for stacks with double coated electrodes. No information provided is marked with (-).

No.	Ref.	Interfaces in R_c	Dry / wet	$\frac{p}{\mathrm{bar}}$	$\frac{T}{\mathrm{K}}$	$\frac{R_c}{\mathrm{cm}^2\ \mathrm{K\ W}^{-1}}$	$\frac{\sum R_c}{\mathrm{cm}^2\ \mathrm{K\ W}^{-1}}$
4	[135]	Graphite/Cu	Wet	-	-	0.77 ± 0.04	-
5	[135]	Graphite/Cu	Dry	-	-	2.28 ± 0.22	-
6	[135]	NMC/Cu	Wet	-	-	1.17 ± 0.14	-
7	[135]	NMC/Cu	Dry	-	-	4.84 ± 0.07	-

8	[135]	Separator/NMC Separator/Graphite	Dry	0.34	298	4.76 ± 0.4	9.52
9	[135]	Separator/NMC Separator/Graphite	Wet	0.34	298	2.47 ± 1.4	4.94
10	[152]	Separator/LCO	Dry	-	300	4.20	8.4 a)b)
11	[152]	Separator/LCO c)	Dry	-	300	0.90	1.8 a)b)
12	[155]	Cu/Graphite Graphite/Separator Separator/LCO LCO/Cu	Wet	8.6 ±8.6	>263	3.48 ±0.79	-

a) Thermal contact resistance of coating-collector interface is neglected. b) Thermal contact resistance of anode coating to separator is neglected.
c) Separator with amine-based chemical bridging of the interface.

In summary, the total thermal contact resistance between the stacked stack layers in Equation (10) $\sum R_c$ appears to have a dominant influence on the total through-plane conductivity $k_\perp$. However, compared to other thermophysical properties, $\sum R_c$ is less studied in the literature. In particular, *in-situ* measurements with full-cells of different formats, comparable to the investigations by Lubner et al. [135], could explain different findings for $k_\perp$. In addition, the correlation of $\sum R_c$ with pressure, temperature, and SOH also needs to be better understood.

4. Conclusion

This article gives an overview of heat capacity and thermal conductivity measurements on cell components and complete lithium-ion cells. To facilitate the parameterization of thermal cell models, this paper calculates recommended medians for both thermal parameters. Furthermore, parameter uncertainties are given which can be used for the error estimation of thermal simulations. The correlation between thermal parameters and common battery states such as temperature, SOC and SOH is also examined. In addition, this review paper reveals missing experiments and gives implication for battery design. A summary of the results is shown in Figure 8.

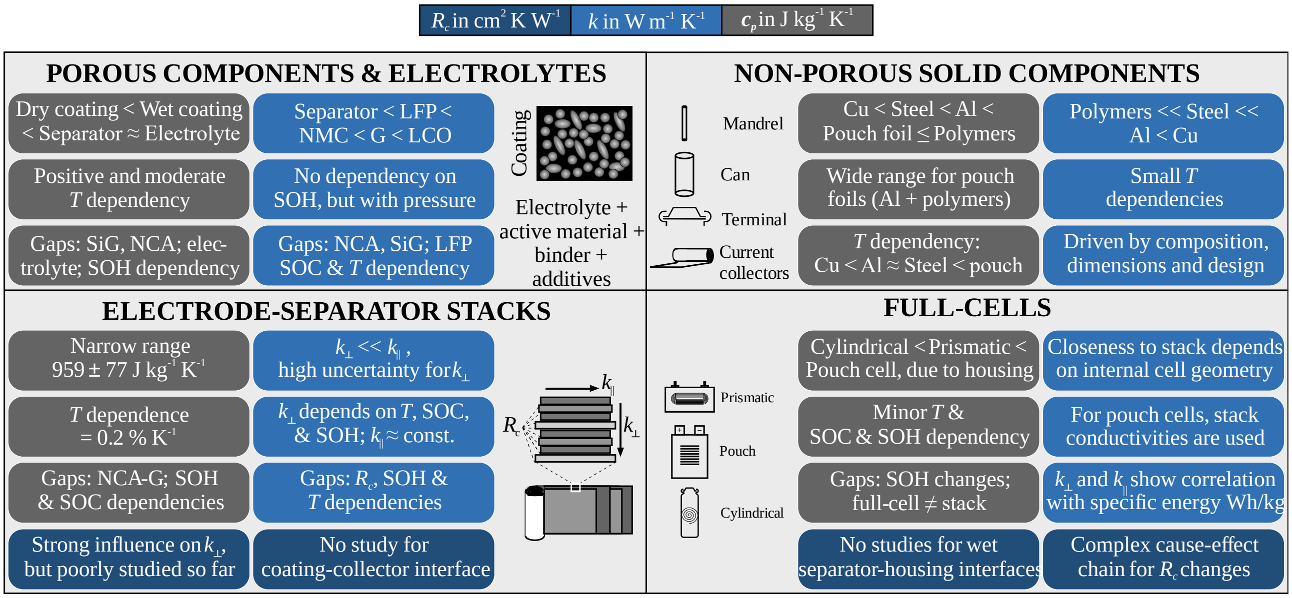

Figure 8: Summary figure that describes the most important results of this meta-analysis for thermal parameters of lithium-ion cells and their components.

4.1. Specific heat capacity

The following conclusion can be drawn for the specific heat capacity of non-porous and porous cell components:

- The electrolyte and dry separator sheets have the highest median heat capacity between 1635 and 1600 J kg^{-1} K^{-1}. Dry anode coatings, cathode coatings and aluminum collectors have a median heat capacity of 718, 764 and 884 J kg^{-1} K^{-1}, respectively. Copper collectors and steel housings introduce the lowest median heat capacity between 387 and 480 J kg^{-1} K^{-1}.
- The specific heat capacity of stack layers is either not correlated with the temperature or is positively correlated (0.0 to 0.5% K^{-1}). The correlation of SOH or SOC with specific heat capacity has seldom been investigated for stack layers, probably because a characterization would require the disassembly of many cells in different SOHs or SOCs. The few results show either a positive or a negative SOC dependency, while no results are available for the SOH.
- There is a large uncertainty for the heat capacity of the electrolyte of ±80%, which means that further measurements are required to identify outliers and narrow the value range. In addition, no heat capacity experiments were found for dry LTO, silicon-graphite and NCA coatings.

The following conclusion can be drawn for the specific heat capacity of the electrode-separator stack:

- The specific heat capacity of the wet electrode-separator stack shows a slight variation between different stack designs and chemistries of ±77 $\mathrm{J\,kg^{-1}\,K^{-1}}$ with a median of 959 $\mathrm{J\,kg^{-1}\,K^{-1}}$. Variations are caused, for example, by the strong correlation between the coating-collector thickness ratio of the anode and the heat capacity of the stack.
- The temperature dependence of the stack capacity is 0.2% $\mathrm{K^{-1}}$, which corresponds to the temperature dependence of dry cathode coatings for lithium-ion cells.
- Further measurements are required to determine the dependencies of SOC or SOH at the stack level. In addition, no measurements for NCA-G stacks are published in the literature.

The following conclusion can be drawn for the specific heat capacity full-cells:

- The heat capacity of the full-cell depends heavily on the cell format, which can be explained by the mass fraction of the cell housing. The housing material is responsible for the fact that cylindrical cells (912 $\mathrm{J\,kg^{-1}\,K^{-1}}$) have a lower heat capacity than prismatic cells (1041 $\mathrm{J\,kg^{-1}\,K^{-1}}$) and prismatic cells have a lower heat capacity than pouch cells (1168 $\mathrm{J\,kg^{-1}\,K^{-1}}$).
- The temperature dependence has been well studied with an order of magnitude equal to that of dry cathode coatings. The heat capacity of the full-cell shows a minor SOC dependency between -4% and 7%. In addition, a positive correlation between the specific energy and the specific heat capacity of full-cells can be determined, which is due to a reduced mass fraction of the copper current collectors and cell housing.
- Further experimentation at the stack and full cell level is required to resolve the discrepancy between the measured heat capacity at the stack and the full-cell level. Moreover, the correlation between the heat capacity of the full-cell and the SOH needs to be deeply studied. Only one study is published and this study did not reveal any correlation between the heat capacity of full cells and the SOH.

4.2. Thermal conductivity

The following conclusion can be drawn for the in-plane thermal conductivity of the electrode-separator stack and full-cells:

- The in-plane conductivity ranges within 21 and 40.1 $\mathrm{W\,m^{-1}\,K^{-1}}$. Compared to the through-plane conductivity, the in-plane conductivity has a smaller uncertainty and is measured less often in the literature.

- The in-plane conductivity shows a weak negative dependency on SOC, a negligible influence of the temperature, and an unknown relation with SOH. In addition, the measurements indicate a negative correlation between the specific energy of the cell and the in-plane conductivity.
- Experiments for stacks with a NCA cathode or LTO anode are missing for the in-plane conductivity.

The following conclusion can be drawn for the through-plane thermal conductivity of the electrode-separator stack and full-cells:

- The through-plane conductivity of electrode-separator stacks and full-cells is between 0.15 and $1.4\,\mathrm{W\,m^{-1}\,K^{-1}}$. The uncertainty of the through-plane conductivity is therefore 81% if the cathode chemistry and the layer thicknesses of the electrode-separators stack are unknown. The high uncertainty likely results from variations in structural parameters such as porosity or thermal contact resistance between the layers.
- In contrast to the in-plane conductivity, the through-plane conductivity shows a dependency on the active material. NMC-G stacks, for example, exceed the median through-plane conductivity of LFP-G by more than 296%. The through-plane conductivity changes between -7% and +33% when the SOC is increased from 0% to 100%. A decrease in SOH significantly reduces the through-plane conductivity, but this statement is only supported by two experimental studies.
- Further tests with specified porosities and layer thicknesses are necessary to quantify the influence of the thermal contact resistance. With regard to temperature dependency, conflicting results have been obtained in the literature, suggesting either a positive or a negative correlation. Therefore, further experiments are needed to correlate the SOH and temperature with the through-plane conductivity.

The following conclusion can be drawn for the thermal conductivity of non-porous and porous cell components:

- The conductivity of all measured stack layers is in the range from 0.12 and $1.58\,\mathrm{W\,m^{-1}\,K^{-1}}$ with a strong dependence on the material. The uncertainty for the thermal conductivity of the stack layers lies between 18% and 60%. It should be mentioned that porosity is rarely given in the references, which could be a source of uncertainty.
- The relationship between the temperature or the degree of lithiation and the thermal conductivity of the stack layers has been sparsely researched in the literature. Most stack layers have a slight dependence on pressure and weak dependence on SOH. It

is therefore unlikely that the SOH dependencies observed at full-cell level are caused by the conductivity of the stack layers.

- Concerning the separator, the volume of inorganic materials such as Al_2O_3 seems to have a strong influence on the thermal conductivity, which should be taken into account in the cell design. In addition, the effects of the heat treatment of the graphite coating appear to have a large influence on the thermal conductivity, which requires further experimental investigations. Measurements are missing for LMO, NCA, silicon graphite and LTO. Despite the importance of LFP, there is only one experiment for this cathode coating

Since thermal contact resistances between the stack layers can have a considerable influence on the through-plane conductivity, the test results were summarized in this paper.

- Deviations between the calculated and measured through-plane conductivity indicate a thermal contact resistance between 0.24 and 12.98 $\mathrm{cm^2 K\,W^{-1}}$. This range of values agrees with the only experiment that directly measured a wet contact resistance of 4.94 $\mathrm{cm^2\ W\,K^{-1}}$.
- The paucity of measurements underlines the knowledge gap regarding the thermal contact resistance between the stack layers. In particular, the resistance between the current collector and the active coating has not yet been measured. This can also be found for the thermal contact resistance between the stack and the cell housing, which was not measured for a wet separator interface.

In conclusion, the heat capacity and thermal conductivity of lithium-ion cells were measured at every scale, from the stack layers to the entire full-cell. However, there are still gaps in knowledge for both parameters, exacerbated by the increasing variability of cell designs. For specific heat capacity, further research should focus on the inconsistency between the heat capacity of the stack and the heat capacity of the full cell. With regard to thermal conductivity, there is a need for further research into thermal contact resistance and the dependencies of battery states, particularly SOH. In addition, both thermal parameters must be measured at full cell level for temperatures above the normal operating window, aiming to improve thermal model parameterization in safety simulations.

Acknowledgements

This work was kindly supported by Innovate UK Battery Advanced for Future Transport Applications (BAFTA) project (104428), the EPSRC Faraday Institution's Multi-Scale Modelling Project [EP/S003053/1, grant number FIRG003], the EPSRC Joint UK-India Clean Energy Centre (JUICE) [EP/P003605/1], the EPSRC Integrated Development of Low-Carbon Energy Systems (IDLES) project [EP/R045518/1], and by the German Federal Ministry for Economic Affairs and Energy (BMWi) [03ET6153C iMoBatt].

Nomenclature

Abbreviations

CC	Current collector
CID	Current interrupt device
CRM	Component-resolved models
DMC	Dimethyl carbonate
EC	Ethylene carbonate
EV	Electric vehicles
HFP	Hexafluoropropylene
ICE	Internal combustion engine
LCO	Lithium-cobalt-oxide
LFP	Lithium-iron-phosphate
LMO	Lithium-manganese-oxide
LRM	Layer-resolved models
LTO	Lithium-titanate-oxide
NCA	Lithium-nickel-cobalt-aluminum-oxide
NiMH	Nickel–metal hydride
NMC	Lithium-nickel-manganese-cobalt-oxide
PA	Polyamide
PE	Polyethylene
PET	Polyethylene terephthalate
PP	Polypropylene
PU	Polyester
PVC	Polyvinyl chloride
PVDF	Polyvinylidene fluoride
SDM	Single-domain models
SEI	Solid-electrolyte interface

SOC	State of charge of full-cell
SOH	State of health of full-cell

Greek symbols and units

$\alpha_{c_p,T}$	% K^{-1}	Temperature dependency of specific heat capacity
$\alpha_{c_p,SOC}$	%	SOC dependency of specific heat capacity
$\alpha_{c_p,SOH}$	%	SOH dependency of specific heat capacity
$\alpha_{k,T}$	% K^{-1}	Temperature dependency of thermal conductivity
$\alpha_{k,SOC}$	%	SOC dependency of thermal conductivity
$\alpha_{k,SOH}$	%	SOH dependency of thermal conductivity
ϵ	%	Porosity of cell layer
ϵ_{ano}	%	Porosity of anode coating
ρ_{solid}	g cm^{-3}	Density of solid phase of porous material
ρ_{fluid}	g cm^{-3}	Density of fluid phase of porous material
ρ_{bulk}	g cm^{-3}	Density of porous material
$\rho_{scm,i}$	g cm^{-3}	Density of subcomponent inside the solid phase of porous material i

Latin symbols and units

A_{surf}	m^2	Cell surface area
c_{por}	J kg^{-1} K^{-1}	Specific heat capacity of porous material
c_{stack}	J kg^{-1} K^{-1}	Specific heat capacity of the electrode-separator stack
c_{cell}	J kg^{-1} K^{-1}	Specific heat capacity of the full-cell
c_{solid}	J kg^{-1} K^{-1}	Specific heat capacity of solid phase inside porous material
c_{fluid}	J kg^{-1} K^{-1}	Specific heat capacity of fluid phase inside porous material
c_n	J kg^{-1} K^{-1}	Specific heat capacity of solid components outside the electrode-separator stack
c_{ano}	J kg^{-1} K^{-1}	Specific heat capacity of dry anode coating
c_{cat}	J kg^{-1} K^{-1}	Specific heat capacity of dry cathode coating
c_{aCC}	J kg^{-1} K^{-1}	Specific heat capacity of anode current collector
c_{cCC}	J kg^{-1} K^{-1}	Specific heat capacity of cathode current collector
c_{sep}	J kg^{-1} K^{-1}	Specific heat capacity of the dry separator
c_{ele}	J kg^{-1} K^{-1}	Specific heat capacity of the electrolyte
c_m	J kg^{-1} K^{-1}	Molar heat capacity
c_p	J kg^{-1} K^{-1}	Specific heat capacity at constant pressure
c_{scmi}	J kg^{-1} K^{-1}	Specific heat capacity of subcomponent inside the solid phase of porous material i
$d_{l,i}$	m	Thickness of layer inside the electrode-separator stack

d_{ano}	m	Thickness of anode coating
d_{aCC}	m	Thickness of anode current collector
d_{cat}	m	Thickness of cathode coating
d_{cCC}	m	Thickness of cathode current collector
d_{sep}	m	Thickness of separator
e_{cell}	$\mathrm{Wh\ kg^{-1}}$	Specific energy of the cell
h_{surf}	$\mathrm{W\ m^{-2}\ K^{-1}}$	Heat transfer coefficient at the outer surface of the cell
k_x	$\mathrm{W\ m^{-1}\ K^{-1}}$	Thermal conductivity in x-axis direction
k_y	$\mathrm{W\ m^{-1}\ K^{-1}}$	Thermal conductivity in y-axis direction
k_z	$\mathrm{W\ m^{-1}\ K^{-1}}$	Thermal conductivity in z-axis direction
k_l	$\mathrm{W\ m^{-1}\ K^{-1}}$	Thermal conductivity of the electrode-separator stack layer
$k_{\parallel}$	$\mathrm{W\ m^{-1}\ K^{-1}}$	Thermal conductivity in in-plane direction of the electrode-separator stack
$k_{\perp}$	$\mathrm{W\ m^{-1}\ K^{-1}}$	Thermal conductivity in through-plane direction of the electrode-separator stack
k_s	$\mathrm{W\ m^{-1}\ K^{-1}}$	Thermal conductivity of solid non-porous components
m_{cell}	kg	Mass of full-cell
m_{ano}	kg	Mass of dry anode coating
m_{cat}	kg	Mass of dry cathode coating
m_{aCC}	kg	Mass of anode current collector
m_{cCC}	kg	Mass of cathode current collector
m_{sep}	kg	Mass of dry separator
m_n	kg	Mass of cell components outside the electrode-separator stack
m_{stack}	kg	Mass of electrode-separator stack
$m_{scm,i}$	kg	Mass subcomponent inside the solid phase of porous materia
m_c	kg	Mass of cell component
$\dot{q}$	$\mathrm{W\ m^{-3}}$	Heat generation inside the cell
Q_{cell}	Ah	Nominal capacity of the full-cell
T_{cell}	K	cell temperature
T_{amb}	K	Ambient temperature
U_{cell}	V	Nominal voltage of the cell
V_{cell}	$\mathrm{m^3}$	Cell volume
p	bar	Pressure during the measurement
$R_{c,i}$	$\mathrm{cm^2\ K\ W^{-1}}$	Thermal contact resistance of interface i

References

[1] A. Arya, A.L. Sharma, A glimpse on all-solid-state Li-ion battery (ASSLIB) performance based on novel solid polymer electrolytes: a topical review, J Mater Sci 55 (2020) 6242–6304. https://doi.org/10.1007/s10853-020-04434-8.

[2] T.M. Bandhauer, S. Garimella, T.F. Fuller, A Critical Review of Thermal Issues in Lithium-Ion Batteries, J. Electrochem. Soc. 158 (2011) R1. https://doi.org/10.1149/1.3515880.

[3] Y. Zhao, O. Pohl, A.I. Bhatt, G.E. Collis, P.J. Mahon, T. Rüther, A.F. Hollenkamp, A Review on Battery Market Trends, Second-Life Reuse, and Recycling, Sustainable Chemistry 2 (2021) 167–205. https://doi.org/10.3390/suschem2010011.

[4] J.J. Gómez Vilchez, P. Jochem, Powertrain technologies and their impact on greenhouse gas emissions in key car markets, Transportation Research Part D: Transport and Environment 80 (2020) 102214. https://doi.org/10.1016/j.trd.2019.102214.

[5] Y. Liu, Y. Zhu, Y. Cui, Challenges and opportunities towards fast-charging battery materials, Nat Energy 4 (2019) 540–550. https://doi.org/10.1038/s41560-019-0405-3.

[6] L. Kraft, A. Hoefling, T. Zünd, A. Kunz, M. Steinhardt, J. Tübke, A. Jossen, Implications of the Heat Generation of LMR-NCM on the Thermal Behavior of Large-Format Lithium-Ion Batteries, J. Electrochem. Soc. 168 (2021) 53505. https://doi.org/10.1149/1945-7111/ac0069.

[7] J.V. Barreras, R. de Castro, Y. Wan, T. Dragicevic, A Consensus Algorithm for Multi-Objective Battery Balancing, Energies 14 (2021) 4279. https://doi.org/10.3390/en14144279.

[8] L. Ahmadi, M. Fowler, S.B. Young, R.A. Fraser, B. Gaffney, S.B. Walker, Energy efficiency of Li-ion battery packs re-used in stationary power applications, Sustainable Energy Technologies and Assessments 8 (2014) 9–17. https://doi.org/10.1016/j.seta.2014.06.006.

[9] T. Waldmann, M. Wilka, M. Kasper, M. Fleischhammer, M. Wohlfahrt-Mehrens, Temperature dependent ageing mechanisms in Lithium-ion batteries – A Post-

Mortem study, J. Power Sources 262 (2014) 129–135. https://doi.org/10.1016/j.jpowsour.2014.03.112.

[10] M. Schimpe, J.V. Barreras, B. Wu, G.J. Offer, Battery Degradation-Aware Current Derating: An Effective Method to Prolong Lifetime and Ease Thermal Management, J. Electrochem. Soc. 168 (2021) 60506. https://doi.org/10.1149/1945-7111/ac0553.

[11] E. Cabrera-Castillo, F. Niedermeier, A. Jossen, Calculation of the state of safety (SOS) for lithium ion batteries, J. Power Sources 324 (2016) 509–520. https://doi.org/10.1016/j.jpowsour.2016.05.068.

[12] J. Warner, The handbook of lithium-ion battery pack design: Chemistry, components, types and terminology, Elsevier, Amsterdam, 2015.

[13] A. Loges, S. Herberger, P. Seegert, T. Wetzel, A study on specific heat capacities of Li-ion cell components and their influence on thermal management, J. Power Sources 336 (2016) 341–350. https://doi.org/10.1016/j.jpowsour.2016.10.049.

[14] G. Karimi, X. Li, Thermal management of lithium-ion batteries for electric vehicles, Int. J. Energy Res. 37 (2013) 13–24. https://doi.org/10.1002/er.1956.

[15] X.-G. Yang, C.-Y. Wang, Understanding the trilemma of fast charging, energy density and cycle life of lithium-ion batteries, J. Power Sources 402 (2018) 489–498. https://doi.org/10.1016/j.jpowsour.2018.09.069.

[16] M.-T.F. Rodrigues, G. Babu, H. Gullapalli, K. Kalaga, F.N. Sayed, K. Kato, J. Joyner, P.M. Ajayan, A materials perspective on Li-ion batteries at extreme temperatures, Nat Energy 2 (2017). https://doi.org/10.1038/nenergy.2017.108.

[17] J. Park, W.A. Appiah, S. Byun, D. Jin, M.-H. Ryou, Y.M. Lee, Semi-empirical long-term cycle life model coupled with an electrolyte depletion function for large-format graphite/LiFePO 4 lithium-ion batteries, J. Power Sources 365 (2017) 257–265. https://doi.org/10.1016/j.jpowsour.2017.08.094.

[18] X. Feng, M. Ouyang, X. Liu, L. Lu, Y. Xia, X. He, Thermal runaway mechanism of lithium ion battery for electric vehicles: A review: A review, Energy Storage Materials 10 (2018) 246–267. https://doi.org/10.1016/j.ensm.2017.05.013.

[19] R. Spotnitz, J. Franklin, Abuse behavior of high-power, lithium-ion cells, J. Power Sources 113 (2003) 81–100. https://doi.org/10.1016/S0378-7753(02)00488-3.

[20] D.D. MacNeil, D. Larcher, J.R. Dahn, Comparison of the Reactivity of Various Carbon Electrode Materials with Electrolyte at Elevated Temperature, J. Electrochem. Soc. 146 (1999) 3596–3602. https://doi.org/10.1149/1.1392520.

[21] A. Rheinfeld, S. Kosch, S.V. Erhard, P.J. Osswald, B. Rieger, A. Jossen, Electro-Thermal Modeling of Large Format Lithium-Ion Pouch Cells: A Cell Temperature Dependent Linear Polarization Expression, J. Electrochem. Soc. 163 (2016) A3046-A3062. https://doi.org/10.1149/2.0701614jes.

[22] X. Zhang, R. Klein, A. Subbaraman, S. Chumakov, X. Li, J. Christensen, C. Linder, S.U. Kim, Evaluation of convective heat transfer coefficient and specific heat capacity of a lithium-ion battery using infrared camera and lumped capacitance method, J. Power Sources 412 (2019) 552–558. https://doi.org/10.1016/j.jpowsour.2018.11.064.

[23] W. Mei, Q. Duan, W. Lu, J. Sun, Q. Wang, An investigation on expansion behavior of lithium ion battery based on the thermal-mechanical coupling model, Journal of Cleaner Production 274 (2020) 122643. https://doi.org/10.1016/j.jclepro.2020.122643.

[24] X. Feng, L. Lu, M. Ouyang, J. Li, X. He, A 3D thermal runaway propagation model for a large format lithium ion battery module, Energy 115 (2016) 194–208. https://doi.org/10.1016/j.energy.2016.08.094.

[25] X.-G. Yang, G. Zhang, C.-Y. Wang, Computational design and refinement of self-heating lithium ion batteries, J. Power Sources 328 (2016) 203–211. https://doi.org/10.1016/j.jpowsour.2016.08.028.

[26] J. Sturm, A. Frank, A. Rheinfeld, S.V. Erhard, A. Jossen, Impact of Electrode and Cell Design on Fast Charging Capabilities of Cylindrical Lithium-Ion Batteries, J. Electrochem. Soc. 167 (2020) 130505. https://doi.org/10.1149/1945-7111/abb40c.

[27] K. Shah, V. Vishwakarma, A. Jain, 2016. Measurement of Multiscale Thermal Transport Phenomena in Li-Ion Cells: A Review. Journal of Electrochemical Energy Conversion and Storage 13, 030801. https://doi.org/10.1115/1.4034413.

[28] S.-C. Chen, Y.-Y. Wang, C.-C. Wan, Thermal Analysis of Spirally Wound Lithium Batteries, J. Electrochem. Soc. 153 (2006) A637. https://doi.org/10.1149/1.2168051.

[29] H. Maleki, S.A. Hallaj, J.R. Selman, R.B. Dinwiddie, B. Wang, Thermal Properties of Lithium-Ion Battery and Components, J. Electrochem. Soc. 146 (1999) 947. https://doi.org/10.1149/1.1391704.

[30] S. Madani, E. Schaltz, S. Knudsen Kær, Review of Parameter Determination for Thermal Modeling of Lithium Ion Batteries, Batteries 4 (2018) 20. https://doi.org/10.3390/batteries4020020.

[31] Y. Tang, T. Li, X. Cheng, Review of Specific Heat Capacity Determination of Lithium-Ion Battery, Energy Procedia 158 (2019) 4967–4973. https://doi.org/10.1016/j.egypro.2019.01.671.

[32] R. Kantharaj, A.M. Marconnet, Heat Generation and Thermal Transport in Lithium-Ion Batteries: A Scale-Bridging Perspective, Nanoscale and Microscale Thermophysical Engineering 23 (2019) 128–156. https://doi.org/10.1080/15567265.2019.1572679.

[33] C.G. Thomas, Research methodology and scientific writing, Second edition, Springer; ANE Books, Cham, India, 2021.

[34] M. Steinhardt, E.I. Gillich, M. Stiegler, A. Jossen, Thermal conductivity inside prismatic lithium-ion cells with dependencies on temperature and external compression pressure, Journal of Energy Storage 32 (2020) 101680. https://doi.org/10.1016/j.est.2020.101680.

[35] M. Guo, R.E. White, Mathematical model for a spirally-wound lithium-ion cell, J. Power Sources 250 (2014) 220–235. https://doi.org/10.1016/j.jpowsour.2013.11.023.

[36] S. Li, N. Kirkaldy, C. Zhang, K. Gopalakrishnan, T. Amietszajew, L.B. Diaz, J.V. Barreras, M. Shams, X. Hua, Y. Patel, G.J. Offer, M. Marinescu, Optimal cell tab design and cooling strategy for cylindrical lithium-ion batteries, J. Power Sources 492 (2021) 229594. https://doi.org/10.1016/j.jpowsour.2021.229594.

[37] J. Yi, U.S. Kim, C.B. Shin, T. Han, S. Park, Three-Dimensional Thermal Modeling of a Lithium-Ion Battery Considering the Combined Effects of the Electrical and Thermal Contact Resistances between Current Collecting Tab and Lead Wire, J. Electrochem. Soc. 160 (2013) A437-A443. https://doi.org/10.1149/2.039303jes.

[38] M. Akbarzadeh, T. Kalogiannis, J. Jaguemont, J. He, L. Jin, M. Berecibar, J. van Mierlo, Thermal modeling of a high-energy prismatic lithium-ion battery cell and

module based on a new thermal characterization methodology, Journal of Energy Storage 32 (2020) 101707. https://doi.org/10.1016/j.est.2020.101707.

[39] A. Rheinfeld, J. Sturm, A. Frank, S. Kosch, S.V. Erhard, A. Jossen, Impact of Cell Size and Format on External Short Circuit Behavior of Lithium-Ion Cells at Varying Cooling Conditions: Modeling and Simulation, J. Electrochem. Soc. 167 (2020) 13511. https://doi.org/10.1149/2.0112001JES.

[40] H. Lundgren, P. Svens, H. Ekström, C. Tengstedt, J. Lindström, M. Behm, G. Lindbergh, Thermal Management of Large-Format Prismatic Lithium-Ion Battery in PHEV Application, J. Electrochem. Soc. 163 (2016) A309-A317. https://doi.org/10.1149/2.09411602jes.

[41] Y. Zhao, Y. Patel, T. Zhang, G.J. Offer, Modeling the Effects of Thermal Gradients Induced by Tab and Surface Cooling on Lithium Ion Cell Performance, J. Electrochem. Soc. 165 (2018) A3169-A3178. https://doi.org/10.1149/2.0901813jes.

[42] C. Forgez, D. Vinh Do, G. Friedrich, M. Morcrette, C. Delacourt, Thermal modeling of a cylindrical LiFePO4/graphite lithium-ion battery, J. Power Sources 195 (2010) 2961–2968. https://doi.org/10.1016/j.jpowsour.2009.10.105.

[43] H. Czichos, T. Saito, L. Smith (Eds.), Springer handbook of materials measurement methods, Springer, Berlin, 2006.

[44] L.’ Kubičár, V. Bohač, V. Vretanár, Š. Barta, G. Neuer, R. Brandt, Thermophysical Properties of Heterogeneous Structures Measured by Pulse Transient Method, Int J Thermophys 26 (2005) 1949–1962. https://doi.org/10.1007/s10765-005-8607-2.

[45] M. Fleckenstein, S. Fischer, O. Bohlen, B. Bäker, Thermal Impedance Spectroscopy - A method for the thermal characterization of high power battery cells, J. Power Sources 223 (2013) 259–267. https://doi.org/10.1016/j.jpowsour.2012.07.144.

[46] P.-L. Lapointe, Application of the thermal impedance spectroscopy method in three dimensions to a large prismatic Li-ion cell, in: 2013 World Electric Vehicle Symposium and Exhibition (EVS27), Barcelona, Spain, IEEE, 2013, pp. 1–6.

[47] E. Barsoukov, J.H. Jang, H. Lee, Thermal impedance spectroscopy for Li-ion batteries using heat-pulse response analysis, J. Power Sources 109 (2002) 313–320. https://doi.org/10.1016/S0378-7753(02)00080-0.

[48] P. Keil, K. Rumpf, A. Jossen, Thermal Impedance Spectroscopy for Li-Ion Batteries with an IR Temperature Sensor System, in: EVS, Barcelona, Spanien, World Electric Vehicle Association, 27 2013.

[49] A. Kwade, W. Haselrieder, R. Leithoff, A. Modlinger, F. Dietrich, K. Droeder, Current status and challenges for automotive battery production technologies, Nat Energy 3 (2018) 290–300. https://doi.org/10.1038/s41560-018-0130-3.

[50] D. Werner, A. Loges, D.J. Becker, T. Wetzel, Thermal conductivity of Li-ion batteries and their electrode configurations – A novel combination of modelling and experimental approach, J. Power Sources 364 (2017) 72–83. https://doi.org/10.1016/j.jpowsour.2017.07.105.

[51] S.S. Zhang, A review on the separators of liquid electrolyte Li-ion batteries, J. Power Sources 164 (2007) 351–364. https://doi.org/10.1016/j.jpowsour.2006.10.065.

[52] F. Richter, S. Kjelstrup, P.J.S. Vie, O.S. Burheim, Thermal conductivity and internal temperature profiles of Li-ion secondary batteries, J. Power Sources 359 (2017) 592–600. https://doi.org/10.1016/j.jpowsour.2017.05.045.

[53] Y. Yang, X. Huang, Z. Cao, G. Chen, Thermally conductive separator with hierarchical nano/microstructures for improving thermal management of batteries, Nano Energy 22 (2016) 301–309. https://doi.org/10.1016/j.nanoen.2016.01.026.

[54] S.C. Chen, C.C. Wan, Y.Y. Wang, Thermal analysis of lithium-ion batteries, J. Power Sources 140 (2005) 111–124. https://doi.org/10.1016/j.jpowsour.2004.05.064.

[55] M. Lewerenz, G. Fuchs, L. Becker, D.U. Sauer, Irreversible calendar aging and quantification of the reversible capacity loss caused by anode overhang, Journal of Energy Storage 18 (2018) 149–159. https://doi.org/10.1016/j.est.2018.04.029.

[56] W. Li, K.R. Crompton, C. Hacker, J.K. Ostanek, Comparison of Current Interrupt Device and Vent Design for 18650 Format Lithium-ion Battery Caps, Journal of Energy Storage 32 (2020) 101890. https://doi.org/10.1016/j.est.2020.101890.

[57] P. Gotcu, W. Pfleging, P. Smyrek, H.J. Seifert, Thermal behaviour of LixMeO2 (Me = Co or Ni + Mn + Co) cathode materials, Phys. Chem. Chem. Phys. 19 (2017) 11920–11930. https://doi.org/10.1039/C7CP00513J.

[58] G. Liebig, U. Kirstein, S. Geißendörfer, F. Schuldt, C. Agert, The Impact of Environmental Factors on the Thermal Characteristic of a Lithium–ion Battery, Batteries 6 (2020) 3. https://doi.org/10.3390/batteries6010003.

[59] P. Bohn, G. Liebig, L. Komsiyska, G. Wittstock, Temperature propagation in prismatic lithium-ion-cells after short term thermal stress, J. Power Sources 313 (2016) 30–36. https://doi.org/10.1016/j.jpowsour.2016.02.055.

[60] U. Seong Kim, J. Yi, C.B. Shin, T. Han, S. Park, Modeling the Dependence of the Discharge Behavior of a Lithium-Ion Battery on the Environmental Temperature, J. Electrochem. Soc. 158 (2011) A611. https://doi.org/10.1149/1.3565179.

[61] V. Vishwakarma, A. Jain, Measurement of in-plane thermal conductivity and heat capacity of separator in Li-ion cells using a transient DC heating method, J. Power Sources 272 (2014) 378–385. https://doi.org/10.1016/j.jpowsour.2014.08.066.

[62] P. Gotcu, H.J. Seifert, Thermophysical properties of $LiCoO_2$-$LiMn_2O_4$ blended electrode materials for Li-ion batteries, Phys. Chem. Chem. Phys. 18 (2016) 10550–10562. https://doi.org/10.1039/c6cp00887a.

[63] J. Nanda, S.K. Martha, W.D. Porter, H. Wang, N.J. Dudney, M.D. Radin, D.J. Siegel, Thermophysical properties of LiFePO4 cathodes with carbonized pitch coatings and organic binders: Experiments and first-principles modeling, J. Power Sources 251 (2014) 8–13. https://doi.org/10.1016/j.jpowsour.2013.11.022.

[64] C. Heumann, Introduction to Statistics and Data Analysis: With Exercises, Solutions and Applications in R, Springer, Cham, 2016.

[65] W.J. Peppel, Preparation and Properties of the Alkylene Carbonates, Ind. Eng. Chem. 50 (1958) 767–770. https://doi.org/10.1021/ie50581a030.

[66] F. Comelli, A. Bigi, D. Vitalini, K. Rubini, Densities, Viscosities, Refractive Indices, and Heat Capacities of Poly(ethylene glycol- ran -propylene glycol) + Esters of Carbonic Acid at (293.15 and 313.15) K and at Atmospheric Pressure, J. Chem. Eng. Data 55 (2010) 205–210. https://doi.org/10.1021/je900307z.

[67] Verein Deutscher Ingenieure, VDI-Gesellschaft Verfahrenstechnik und Chemieingenieurwesen, VDI-Wärmeatlas: Mit 320 Tabellen, eleventh., bearb. und erw. Aufl., Springer Vieweg, Berlin, 2013.

[68] M. Singh, J. Kaiser, H. Hahn, Thick Electrodes for High Energy Lithium Ion Batteries, J. Electrochem. Soc. 162 (2015) A1196-A1201. https://doi.org/10.1149/2.0401507jes.

[69] U. Gaur, S.-f. Lau, B.B. Wunderlich, B. Wunderlich, Heat Capacity and Other Thermodynamic Properties of Linear Macromolecules. VIII. Polyesters and Polyamides, Journal of Physical and Chemical Reference Data 12 (1983) 65–89. https://doi.org/10.1063/1.555678.

[70] U. Gaur, B. Wunderlich, Heat capacity and other thermodynamic properties of linear macromolecules. II. Polyethylene, Journal of Physical and Chemical Reference Data 10 (1981) 119–152. https://doi.org/10.1063/1.555636.

[71] J.E. Mark, Physical properties of polymers handbook, second. ed., Springer Science+Business Media LLC, New York, NY, 2007.

[72] D. Oehler, J. Bender, P. Seegert, T. Wetzel, Investigation of the Effective Thermal Conductivity of Cell Stacks of Li-Ion Batteries, Energy Technology (2020) 2000722. https://doi.org/10.1002/ente.202000722.

[73] S. Picard, D.T. Burns, P. Roger, Determination of the specific heat capacity of a graphite sample using absolute and differential methods, Metrologia 44 (2007) 294–302. https://doi.org/10.1088/0026-1394/44/5/005.

[74] T. Aree, H.-B. Bürgi, Specific heat of molecular crystals from atomic mean square displacements with the Einstein, Debye, and Nernst-Lindemann models, J. Phys. Chem. B 110 (2006) 26129–26134. https://doi.org/10.1021/jp0636322.

[75] Y.S. Touloukian, E.H. Buyco, Specific Heat - Metallic Elements and Alloys, in: Defense Technical Information Center (Ed.), Thermophysical Properties of Matter, 1970.

[76] D.R. Lide, CRC handbook of chemistry and physics, 2003-2004: A ready-reference book of chemical and physical data, eighthfourthth ed., CRC Press, Boca Raton, Fla., 2003.

[77] T. Bandhauer, S. Garimella, T.F. Fuller, Electrochemical-Thermal Modeling to Evaluate Battery Thermal Management Strategies: I. Side Cooling, J. Electrochem. Soc. 162 (2015) A125-A136. https://doi.org/10.1149/2.0571501jes.

[78] L. Sheng, L. Su, H. Zhang, Experimental determination on thermal parameters of prismatic lithium ion battery cells, International Journal of Heat and Mass Transfer 139 (2019) 231–239. https://doi.org/10.1016/j.ijheatmasstransfer.2019.04.143.

[79] L. Sheng, Z. Zhang, L. Su, H. Zhang, H. Zhang, Y. Fang, K. Li, W. Ye, Quasi steady state method to measure thermophysical parameters of cylindrical lithium ion batteries, J. Power Sources 485 (2021) 229342. https://doi.org/10.1016/j.jpowsour.2020.229342.

[80] P.J. Osswald, S.V. Erhard, A. Noel, P. Keil, F.M. Kindermann, H. Hoster, A. Jossen, Current density distribution in cylindrical Li-Ion cells during impedance measurements, J. Power Sources 314 (2016) 93–101. https://doi.org/10.1016/j.jpowsour.2016.02.070.

[81] A. Petit, P.L. Dulong, Recherches sur quelques points importants de la théorie de la chaleur., Annales de chimie et de physique (1819) 395–413.

[82] U. Grigull, W. Blanke, Thermophysikalische Stoffgrößen, Springer Berlin Heidelberg, Berlin, Heidelberg, 1989.

[83] Y. Saito, K. Kanari, K. Takano, T. Masuda, A calorimetric study on a cylindrical type lithium secondary battery by using a twin-type heat conduction calorimeter, Thermochimica Acta 296 (1997) 75–85. https://doi.org/10.1016/S0040-6031(97)00083-X.

[84] W. Hesse, Aluminium-Werkstoff-Datenblätter: Deutsch, seventhth ed., Beuth Verlag GmbH, Berlin, 2016.

[85] Y.S. Touloukian, C.Y. Ho, Part II: Thermophyslcal Properties of Seven Materials, in: Defense Technical Information Center (Ed.), THERMOPHYSICAL PROPERTIES OF SELECTED AEROSPACE MATERIALS, 1977.

[86] R.H. Bogaard, P.D. Desai, H.H. Li, C.Y. Ho, Thermophysical properties of stainless steels, Thermochimica Acta 218 (1993) 373–393. https://doi.org/10.1016/0040-6031(93)80437-F.

[87] K.A. Murashko, A.V. Mityakov, J. Pyrhönen, V.Y. Mityakov, S.S. Sapozhnikov, Thermal parameters determination of battery cells by local heat flux

measurements, J. Power Sources 271 (2014) 48–54. https://doi.org/10.1016/j.jpowsour.2014.07.117.

[88] M. Shadman Rad, D.L. Danilov, M. Baghalha, M. Kazemeini, P.H.L. Notten, Adaptive thermal modeling of Li-ion batteries, Electrochimica Acta 102 (2013) 183–195. https://doi.org/10.1016/j.electacta.2013.03.167.

[89] C. Vargel, Corrosion of aluminium, first. ed., Elsevier, Amsterdam, 2004.

[90] J. Zhang, B. Wu, Z. Li, J. Huang, Simultaneous estimation of thermal parameters for large-format laminated lithium-ion batteries, J. Power Sources 259 (2014) 106–116. https://doi.org/10.1016/j.jpowsour.2014.02.079.

[91] A.W. Golubkov, D. Fuchs, J. Wagner, H. Wiltsche, C. Stangl, G. Fauler, G. Voitic, A. Thaler, V. Hacker, Thermal-runaway experiments on consumer Li-ion batteries with metal-oxide and olivin-type cathodes, RSC Adv 4 (2014) 3633–3642. https://doi.org/10.1039/C3RA45748F.

[92] A.W. Golubkov, S. Scheikl, R. Planteu, G. Voitic, H. Wiltsche, C. Stangl, G. Fauler, A. Thaler, V. Hacker, Thermal runaway of commercial 18650 Li-ion batteries with LFP and NCA cathodes – impact of state of charge and overcharge, RSC Adv 5 (2015) 57171–57186. https://doi.org/10.1039/c5ra05897j.

[93] C. Essl, A.W. Golubkov, E. Gasser, M. Nachtnebel, A. Zankel, E. Ewert, A. Fuchs, Comprehensive Hazard Analysis of Failing Automotive Lithium-Ion Batteries in Overtemperature Experiments, Batteries 6 (2020) 30. https://doi.org/10.3390/batteries6020030.

[94] J. Marshall, D. Gastol, R. Sommerville, B. Middleton, V. Goodship, E. Kendrick, Disassembly of Li Ion Cells—Characterization and Safety Considerations of a Recycling Scheme, Metals 10 (2020) 773. https://doi.org/10.3390/met10060773.

[95] Di Pan, H. Guo, S. Tang, X. Li, Z. Wang, W. Peng, J. Wang, G. Yan, Evaluating the accuracy of electro-thermal coupling model in lithium-ion battery via altering internal resistance acquisition methods, J. Power Sources 463 (2020) 228174. https://doi.org/10.1016/j.jpowsour.2020.228174.

[96] X. Cheng, Y. Tang, Z. Wang, Thermal Property Measurements of a Large Prismatic Lithium-ion Battery for Electric Vehicles, J. Therm. Sci. (2021). https://doi.org/10.1007/s11630-021-1398-3.

[97] R. Zhao, J. Liu, J. Gu, The effects of electrode thickness on the electrochemical and thermal characteristics of lithium ion battery, Applied Energy 139 (2015) 220–229. https://doi.org/10.1016/j.apenergy.2014.11.051.

[98] M. Steinhardt, E.I. Gillich, A. Rheinfeld, L. Kraft, M. Spielbauer, O. Bohlen, A. Jossen, Low-effort determination of heat capacity and thermal conductivity for cylindrical 18650 and 21700 lithium-ion cells, Journal of Energy Storage 42 (2021) 103065. https://doi.org/10.1016/j.est.2021.103065.

[99] J. Geder, R. Arunachala, S. Jairam, A. Jossen, Thermal behavior of aged lithium-ion batteries: calorimetric observations, in: 2015 IEEE Green Energy and Systems Conference (IGESC), Long Beach, CA, USA, pp. 24–29.

[100] S.J. Bazinski, X. Wang, Experimental study on the influence of temperature and state-of-charge on the thermophysical properties of an LFP pouch cell, J. Power Sources 293 (2015) 283–291. https://doi.org/10.1016/j.jpowsour.2015.05.084.

[101] G. Vertiz, M. Oyarbide, H. Macicior, O. Miguel, I. Cantero, P. Fernandez de Arroiabe, I. Ulacia, Thermal characterization of large size lithium-ion pouch cell based on 1d electro-thermal model, J. Power Sources 272 (2014) 476–484. https://doi.org/10.1016/j.jpowsour.2014.08.092.

[102] M.B. Ahmed, S. Shaik, A. Jain, Measurement of radial thermal conductivity of a cylinder using a time-varying heat flux method, International Journal of Thermal Sciences 129 (2018) 301–308. https://doi.org/10.1016/j.ijthermalsci.2018.03.008.

[103] A.A. Pesaran, M. Keyser, Thermal characteristics of selected EV and HEV batteries, in: 2001 16th Annual Battery Conference on Applications and Advances, Long Beach, CA, USA, I E E E, Piscataway, Jan. 2001, pp. 219–225.

[104] T.S. Bryden, B. Dimitrov, G. Hilton, C. Ponce de León, P. Bugryniec, S. Brown, D. Cumming, A. Cruden, Methodology to determine the heat capacity of lithium-ion cells, J. Power Sources 395 (2018) 369–378. https://doi.org/10.1016/j.jpowsour.2018.05.084.

[105] M. Al-Zareer, A. Michalak, C. Da Silva, C.H. Amon, Predicting specific heat capacity and directional thermal conductivities of cylindrical lithium-ion batteries: A combined experimental and simulation framework, Applied Thermal Engineering 182 (2021) 116075. https://doi.org/10.1016/j.applthermaleng.2020.116075.

[106] X. Liu, Z. Wu, S.I. Stoliarov, M. Denlinger, A. Masias, K. Snyder, Heat release during thermally-induced failure of a lithium ion battery: Impact of cathode composition, Fire Safety Journal 85 (2016) 10–22. https://doi.org/10.1016/j.firesaf.2016.08.001.

[107] C. Lin, H. Wen, L. Liu, S. Liu, T. Ma, B. Fan, F. Wang, Heat generation quantification of high-specific-energy 21700 battery cell using average and variable specific heat capacities, Applied Thermal Engineering 184 (2021) 116215. https://doi.org/10.1016/j.applthermaleng.2020.116215.

[108] K. Murashko, D. Li, D.L. Danilov, P.H.L. Notten, J. Pyrhönen, J. Jokiniemi, Applicability of Heat Generation Data in Determining the Degradation Mechanisms of Cylindrical Li-Ion Batteries, J. Electrochem. Soc. 168 (2021) 10511. https://doi.org/10.1149/1945-7111/abd832.

[109] S.J. Drake, D.A. Wetz, J.K. Ostanek, S.P. Miller, J.M. Heinzel, A. Jain, Measurement of anisotropic thermophysical properties of cylindrical Li-ion cells, J. Power Sources 252 (2014) 298–304. https://doi.org/10.1016/j.jpowsour.2013.11.107.

[110] K.A. Murashko, J. Pyrhönen, J. Jokiniemi, Determination of the through-plane thermal conductivity and specific heat capacity of a Li-ion cylindrical cell, International Journal of Heat and Mass Transfer 162 (2020) 120330. https://doi.org/10.1016/j.ijheatmasstransfer.2020.120330.

[111] L.H. Saw, H.M. Poon, H.S. Thiam, Z. Cai, W.T. Chong, N.A. Pambudi, Y.J. King, Novel thermal management system using mist cooling for lithium-ion battery packs, Applied Energy 223 (2018) 146–158. https://doi.org/10.1016/j.apenergy.2018.04.042.

[112] N.S. Spinner, R. Mazurick, A. Brandon, S.L. Rose-Pehrsson, S.G. Tuttle, Analytical, Numerical and Experimental Determination of Thermophysical Properties of Commercial 18650 LiCoO 2 Lithium-Ion Battery, J. Electrochem. Soc. 162 (2015) A2789-A2795. https://doi.org/10.1149/2.0871514jes.

[113] J.-S. Hong, H. Maleki, S. Al Hallaj, L. Redey, J.R. Selman, Electrochemical-Calorimetric Studies of Lithium-Ion Cells, J. Electrochem. Soc. 145 (1998) 1489–1501. https://doi.org/10.1149/1.1838509.

[114] H. Ruan, J. Jiang, B. Sun, W. Gao, L. Wang, W. Zhang, Online estimation of thermal parameters based on a reduced wide-temperature-range electro-thermal coupled model for lithium-ion batteries, J. Power Sources 396 (2018) 715–724. https://doi.org/10.1016/j.jpowsour.2018.03.075.

[115] J.V. Barreras, C. Fleischer, A.E. Christensen, M. Swierczynski, E. Schaltz, S.J. Andreasen, D.U. Sauer, An Advanced HIL Simulation Battery Model for Battery Management System Testing, IEEE Trans. on Ind. Applicat. 52 (2016) 5086–5099. https://doi.org/10.1109/TIA.2016.2585539.

[116] A. Eddahech, O. Briat, J.-M. Vinassa, Thermal characterization of a high-power lithium-ion battery: Potentiometric and calorimetric measurement of entropy changes, Energy 61 (2013) 432–439. https://doi.org/10.1016/j.energy.2013.09.028.

[117] E. Schuster, C. Ziebert, A. Melcher, M. Rohde, H.J. Seifert, Thermal behavior and electrochemical heat generation in a commercial 40 Ah lithium ion pouch cell, J. Power Sources 286 (2015) 580–589. https://doi.org/10.1016/j.jpowsour.2015.03.170.

[118] S. Balkur, N. Roy Chowdhury, J. Groot, T. Thiringer, A cost and time effective novel methodology to determine specific heat capacity of lithium-ion cells, J. Power Sources 500 (2021) 229981. https://doi.org/10.1016/j.jpowsour.2021.229981.

[119] B. Rieger, S.V. Erhard, K. Rumpf, A. Jossen, A New Method to Model the Thickness Change of a Commercial Pouch Cell during Discharge, J. Electrochem. Soc. 163 (2016) A1566-A1575. https://doi.org/10.1149/2.0441608jes.

[120] C.-H. Doh, Y.-C. Ha, S.-w. Eom, Entropy measurement of a large format lithium ion battery and its application to calculate heat generation, Electrochimica Acta 309 (2019) 382–391. https://doi.org/10.1016/j.electacta.2019.04.026.

[121] J. Jaguemont, M. Sokkeh, S. Hosen, L. Jin, G. Qiao, T. Kalogiannis, J. van Mierlo, 1D-Thermal Analysis and Electro-Thermal Modeling of Prismatic-Shape LTO and NMC Batteries, in: 2019 IEEE Vehicle Power and Propulsion Conference (VPPC), Hanoi, Vietnam, IEEE, 14.10.2019 - 17.10.2019, pp. 1–5.

[122] F.J. Günter, C. Burgstaller, F. Konwitschny, G. Reinhart, Influence of the Electrolyte Quantity on Lithium-Ion Cells, J. Electrochem. Soc. 166 (2019) A1709-A1714. https://doi.org/10.1149/2.0121910jes.

[123] S.J. An, J. Li, D. Mohanty, C. Daniel, B.J. Polzin, J.R. Croy, S. E. Trask, D.L. Wood, Correlation of Electrolyte Volume and Electrochemical Performance in Lithium-Ion Pouch Cells with Graphite Anodes and NMC532 Cathodes, J. Electrochem. Soc. 164 (2017) A1195-A1202. https://doi.org/10.1149/2.1131706jes.

[124] R. Rizk, H. Louahlia, H. Gualous, P. Schaetzel, Experimental analysis and transient thermal modelling of a high capacity prismatic lithium-ion battery, International Communications in Heat and Mass Transfer 94 (2018) 115–125. https://doi.org/10.1016/j.icheatmasstransfer.2018.03.018.

[125] F. Richter, P.J.S. Vie, S. Kjelstrup, O.S. Burheim, Measurements of ageing and thermal conductivity in a secondary NMC-hard carbon Li-ion battery and the impact on internal temperature profiles, Electrochimica Acta 250 (2017) 228–237. https://doi.org/10.1016/j.electacta.2017.07.173.

[126] Y. Ye, L.H. Saw, Y. Shi, K. Somasundaram, A.A.O. Tay, Effect of thermal contact resistances on fast charging of large format lithium ion batteries, Electrochimica Acta 134 (2014) 327–337. https://doi.org/10.1016/j.electacta.2014.04.134.

[127] L. Aiello, G. Kovachev, B. Brunnsteiner, M. Schwab, G. Gstrein, W. Sinz, C. Ellersdorfer, In Situ Measurement of Orthotropic Thermal Conductivity on Commercial Pouch Lithium-Ion Batteries with Thermoelectric Device, Batteries 6 (2020) 10. https://doi.org/10.3390/batteries6010010.

[128] S.J. Bazinski, X. Wang, B.P. Sangeorzan, L. Guessous, Measuring and assessing the effective in-plane thermal conductivity of lithium iron phosphate pouch cells, Energy 114 (2016) 1085–1092. https://doi.org/10.1016/j.energy.2016.08.087.

[129] G. Kovachev, A. Astner, G. Gstrein, L. Aiello, J. Hemmer, W. Sinz, C. Ellersdorfer, Thermal Conductivity in Aged Li-Ion Cells under Various Compression Conditions and State-of-Charge, Batteries 7 (2021) 42. https://doi.org/10.3390/batteries7030042.

[130] A. Loges, S. Herberger, D. Werner, T. Wetzel, Thermal characterization of Li-ion cell electrodes by photothermal deflection spectroscopy, J. Power Sources 325 (2016) 104–115. https://doi.org/10.1016/j.jpowsour.2016.05.082.

[131] K.A. Murashko, A.V. Mityakov, V.Y. Mityakov, S.Z. Sapozhnikov, J. Pyrhonen, Heat flux based method for determination of thermal parameters of the cylindrical

Li-ion battery: Uncertainty analysis, in: 2017 19th European Conference on Power Electronics and Applications (EPE'17 ECCE Europe), Warsaw, Poland, IEEE, 2017, P.1-P.10.

[132] Y. Ye, Y. Shi, A.A.O. Tay, Electro-thermal cycle life model for lithium iron phosphate battery, J. Power Sources 217 (2012) 509–518. https://doi.org/10.1016/j.jpowsour.2012.06.055.

[133] W. Ju, C. Zhu, Z. Wei, Intercalated ion tuning of the cross-plane thermal transport properties of graphite, AIP Advances 10 (2020) 95225. https://doi.org/10.1063/5.0023229.

[134] J. Cho, M.D. Losego, H.G. Zhang, H. Kim, J. Zuo, I. Petrov, D.G. Cahill, P.V. Braun, Electrochemically tunable thermal conductivity of lithium cobalt oxide, Nat. Commun. 5 (2014) 4035. https://doi.org/10.1038/ncomms5035.

[135] S.D. Lubner, S. Kaur, Y. Fu, V. Battaglia, R.S. Prasher, Identification and characterization of the dominant thermal resistance in lithium-ion batteries using operando 3-omega sensors, J. Appl. Phys. 127 (2020) 105104. https://doi.org/10.1063/1.5134459.

[136] H. Ibach, H. Lüth, Solid-State Physics: An Introduction to Principles of Materials Science, Second Edition, Springer, Berlin, Heidelberg, 1996.

[137] C.R. Birkl, M.R. Roberts, E. McTurk, P.G. Bruce, D.A. Howey, Degradation diagnostics for lithium ion cells, J. Power Sources 341 (2017) 373–386. https://doi.org/10.1016/j.jpowsour.2016.12.011.

[138] R.H. Bogaard, Thermal Conductivity of Selected Stainless Steels, in: T. Ashworth, D.R. Smith (Eds.), Thermal Conductivity 18, Springer Verlag, Boston, MA, 2012, pp. 175–185.

[139] R.W. Powell, C.Y. Ho, P.E. Liley, Thermal Conductivity of Selected Materials, 1966.

[140] F.C. Chen, Y.M. Poon, C.L. Choy, Thermal diffusivity of polymers by the flash method, Polymer 18 (1977) 129–136. https://doi.org/10.1016/0032-3861(77)90027-1.

[141] D.E. Kline, Thermal conductivity studies of polymers, J. Polym. Sci. 50 (1961) 441–450. https://doi.org/10.1002/pol.1961.1205015413.

[142] O.S. Burheim, M.A. Onsrud, J.G. Pharoah, F. Vullum-Bruer, P.J.S. Vie, Thermal Conductivity, Heat Sources and Temperature Profiles of Li-Ion Batteries, ECS Transactions 58 (2014) 145–171. https://doi.org/10.1149/05848.0145ecst.

[143] D. Oehler, P. Seegert, T. Wetzel, Modeling the Thermal Conductivity of Porous Electrodes of Li-Ion Batteries as a Function of Microstructure Parameters, Energy Technol. (2020) 2000574. https://doi.org/10.1002/ente.202000574.

[144] D.H. Doughty, Vehicle Battery Safety Roadmap Guidance, 2012.

[145] D. Parikh, C.J. Jafta, B.P. Thapaliya, J. Sharma, H.M. Meyer, C. Silkowski, J. Li, Al2O3/TiO2 coated separators: Roll-to-roll processing and implications for improved battery safety and performance, J. Power Sources 507 (2021) 230259. https://doi.org/10.1016/j.jpowsour.2021.230259.

[146] H. Yang, C.N. Savory, B.J. Morgan, D.O. Scanlon, J.M. Skelton, A. Walsh, Chemical Trends in the Lattice Thermal Conductivity of Li(Ni, Mn, Co)O 2 (NMC) Battery Cathodes, Chem. Mater. 32 (2020) 7542–7550. https://doi.org/10.1021/acs.chemmater.0c02908.

[147] A. Vadakkepatt, B. Trembacki, S.R. Mathur, J.Y. Murthy, Bruggeman's Exponents for Effective Thermal Conductivity of Lithium-Ion Battery Electrodes, J. Electrochem. Soc. 163 (2016) A119-A130. https://doi.org/10.1149/2.0151602jes.

[148] C.V. Madhusudana, Thermal Contact Conductance, Springer, New York, NY, 1996.

[149] S.C. Somé, D. Delaunay, V. Gaudefroy, Comparison and validation of thermal contact resistance models at solid–liquid interface taking into account the wettability parameters, Applied Thermal Engineering 61 (2013) 531–540. https://doi.org/10.1016/j.applthermaleng.2013.08.032.

[150] F. Hao, D. Fang, Z. Xu, Thermal transport in crystalline Si/Ge nano-composites: Atomistic simulations and microscopic models, Appl. Phys. Lett. 100 (2012) 91903. https://doi.org/10.1063/1.3688943.

[151] J. He, L. Zhang, L. Liu, Thermal transport in monocrystalline and polycrystalline lithium cobalt oxide, Phys. Chem. Chem. Phys. 21 (2019) 12192–12200. https://doi.org/10.1039/c9cp01585j.

[152] V. Vishwakarma, C. Waghela, Z. Wei, R. Prasher, S.C. Nagpure, J. Li, F. Liu, C. Daniel, A. Jain, Heat transfer enhancement in a lithium-ion cell through improved

material-level thermal transport, J. Power Sources 300 (2015) 123–131. https://doi.org/10.1016/j.jpowsour.2015.09.028.

[153] C. Li, W. Yang, W. He, X. Zhang, J. Zhu, Multifunctional surfactants for synthesizing high-performance energy storage materials, Energy Storage Materials 43 (2021) 1–19. https://doi.org/10.1016/j.ensm.2021.08.033.

[154] A. Gaitonde, A. Nimmagadda, A. Marconnet, Measurement of interfacial thermal conductance in Lithium ion batteries, J. Power Sources 343 (2017) 431–436. https://doi.org/10.1016/j.jpowsour.2017.01.019.

[155] R. Ponnappan, T.S. Ravigururajan, Contact thermal resistance of Li-ion cell electrode stack, J. Power Sources 129 (2004) 7–13. https://doi.org/10.1016/j.jpowsour.2003.11.006.

[156] P. Teertstra, Thermal Conductivity and Contact Resistance Measurements for Adhesives, in: Proceedings of the ASME InterPACK Conference - 2007, Vancouver, British Columbia, Canada, ASME, New York, NY, 2007, pp. 381–388.